University of Central Lancashire
UCLan
Where opportunity creates success
John Tyndall institute, School of Engineering

Deformation modelling of quasi-isotropic aerodynamic components with life cycle predictions

A THESIS SUBMITTED TO THE

UNIVERSITY OF CENTRAL LANCASHIRE

FOR THE DEGREE OF MASTER OF SCIENCE

IN THE JOHN TYNDALL RESEARCH INSTITUTE

SCHOOL OF ENGINEERING

2023

By

Mr A. R. Cushing

BEng(Hons) AMIMechE MIET

G20636424

Abstract

The aim of this thesis is to investigate the performance of wind turbine blades during normal operational loading cases to aid the prediction of life cycles. The main aim of this work is to critically evaluate if these devices are over-engineered to withstand extreme conditions. It is already known that these systems have a number of replacements during their whole life. The rationale for this work is to develop knowledge of the mechanical material properties used for these devices and how applying normal operating loads introduce fatigue within the materials. Using analytic theories such as Classical Lamination, bending, and Runge-Kutta techniques; along with numerical simulations via ANSYS APDL & Workbench to develop representative models and simulations to draw logical conclusions to the proposed scientific hypothesis. The key findings relating to both how wind turbine blade design, materials and behaviour responses to the loading conditions imposed. The findings will enable a deeper knowledge to the wider community, outside of engineering as well as monetary reductions unless extreme events affect the devices structure. The thesis concludes that Classical Lamination Theory can be used for orthotropic models, aerospace token test pieces can be used to determine composite material properties, layup sequencing of composites yields similar results to orthotropic equivalents, the application of twisted sections within the blade geometry increases the structural stiffness of these devices, and stress calculations can be employed irrespective of modelling software.

Declaration

No portion of the work referred to in this thesis has been submitted in support of an application for another degree or qualification of this or any other university or other institute of learning.

Copyright

Acknowledgements

I would like to thank members of the JTi at UCLan, namely Dr Justin Whitty as the leading supervisor of this research including Dr Jules Simo and Prof Brian Henderson as supervisors. Both Mr Nicolas Gaskell and Mr Jamie Mann with the support during the studies with plenty of useful advice during the research. I would also like to extend my thanks to not only my family in the support of this venture, but my partner Miss Aimee Ashworth who has given everything, in terms of support and guidance during this work. I'd also like to extend my thanks to my work colleagues at Wigan & Leigh College.

Contents

List of Figures

List of Tables

Chapter 1

Introduction

Due to the effect of global warming, the implementation of wind power across the globe has become much more proactive by governments and the business sector alike. Since wind can be viewed as almost inexhaustible, wind energy is regarded as a renewable energy source. The turbines used to harness this power are rather complicated devices, essentially converting the linear kinetic energy in the wind into mechanical rational energy which; in-turn is converted into electricity. By far the most important component which performs this principal mechanical energy transfer are the turbine blades. During normal operating conditions the loads applied to the blades are quite modest (compared to say an aircraft wing) though these devices have long operational lifetimes. Additionally, at very high wind speeds (*i.e.* above the cut-off speed of these devices) the blades may be subjected to abnormal loads. Both of these phenomena result in the blades becoming fatigued.

Wind Turbine Blades (WTB) consist of a number of materials layered together to form a structure, *e.g.* glass fibre embedded in to a matrix material [1, 2] usually consisting of epoxy resin, polyester, or vinylester. Furthermore, many of these critical components can become damaged during service; *in-situ* failure has been attributed to: material imperfections, excessive wind speeds, lightening, fatigue, moisture, and environmental effects [3]. Such failure mechanisms lead many blades to become completely unusable when in service. Moreover, since the composite matrix materials are generally constructed from thermosetting polymers they are very difficult to be recycle. This leads to the conjecture that wind energy is less *renewable* than initially thought [4]. One way to counteract this increasing concern is to better understand these aforementioned failure mechanisms. The need for the development of predictive modelling of composite blades in both pristine and fatigued forms, the subject of this proposal, therefore becomes self evident.

1.1 Wind Energy

Wind energy was first used in the mid 1950's, however at the time was deemed inferior to the then emerging fossil fuelled steam engines. Although, by the 1960's the opposite would slowly become apparent. Further, in the 1990's as installation capacity increased five-fold [5]. One of the first prototypes, similar to modern Horizontal-Axis Wind Turbines (HAWT), was installed in St. Albans, UK. This Enfield-Andreau turbine was capable of producing 100kW featured; two 25m hollow blades, an alternator in the base of the tower, and operated by drawing air though the tower expelling it via the blade tips. Thus driving an air turbine linked to the alternator, as shown in Figure 1.1(a) [6]. Towards the end of the 1990's the trend shifted to large, megawatt-sized offshore wind power. This continued into the early twenty first century with manufacturers campaigning for an increase in wind energy through governing polices for more natural resource energy generation. Comparing the design from 1950's to current HAWTs the power output improvements cannot be ignored. Modern designs are capable of generating up to 12MW of power from three 107m blades, this is a new design undergoing testing from General Electric [7], this leads to an increase of almost twelve-fold.

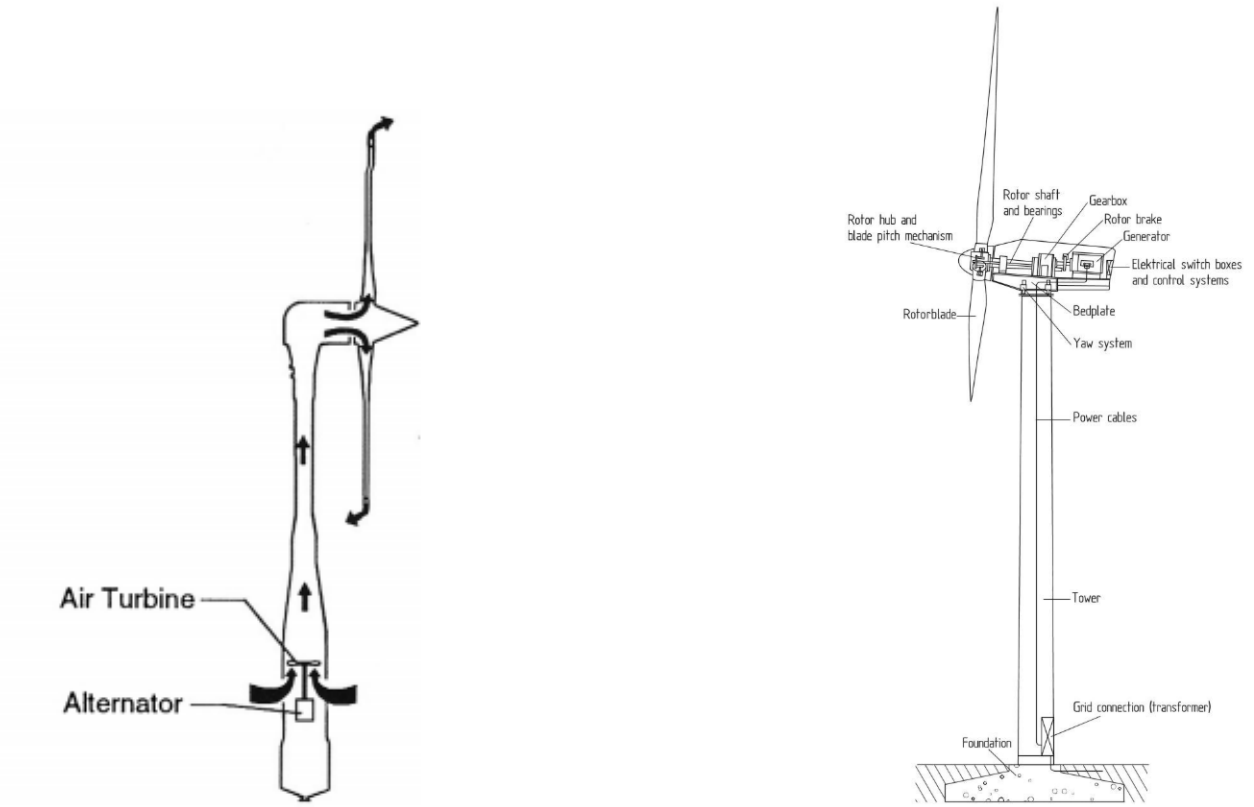

(a) 1950's Design

(b) 2010's Design

Source: [6, 8]

Figure 1.1: Classic and modern wind turbines

Figure 1.2 depicts a basic block diagram of a wind turbine system consisting of the wind turbine, gear box, synchronous generator, and Alternating Current (AC)/Direct Current (DC) and DC/AC converters coupled together with a DC link leading to a step-up transformer to send the power output to the grid.

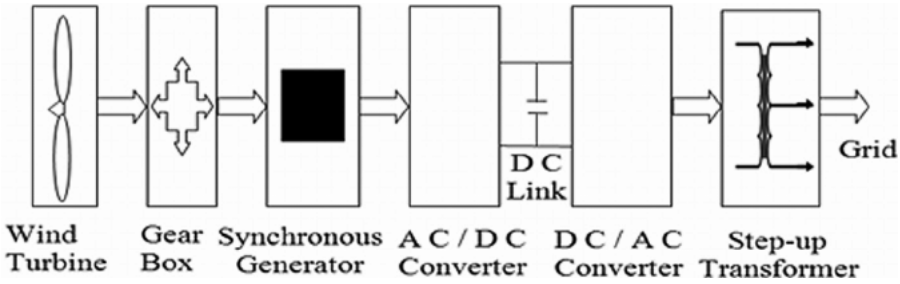

Source: [9]

Figure 1.2: Wind energy block diagram

Wind energy in the United Kingdom is still showing significant growth, as represented in Figure 1.3. Wind energy both onshore and offshore has shown a rapid increase over the last decade. Table 1.1 compares these data to other methods of generating renewable energy and demonstrates that wind power is far greater. Figure 1.3 & Table 1.1 show that 2018 was the United Kingdom's record year for renewable energy generation following an increase of 11.8%. Bioenergy also increased as more power stations are converting to plant biomass, while solar photovoltaic change occurred as a result of increased sunlight hours. Renewable energy generation accounted for 33.3% of all electricity generated by the UK in 2018, an increase of 4.1% from 2017 [10].

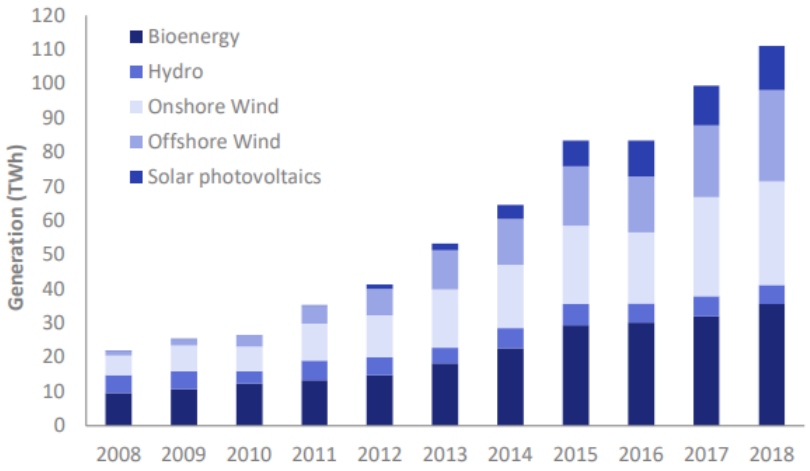

Source: [10]

Figure 1.3: 2018 Renewable energy graph for the United Kingdom

	2018 TWh	Percentage change on a year earlier (%)
Renewable electricity generation		
Onshore wind	30.4	+4.6
Offshore wind	26.7	+27.6
Hydro	5.5	-7.8
Solar PV	12.9	+12.1
Bioenergy	35.6	+11.6
All renewables	111.1	+11.8

Source: [10]

Table 1.1: 2018 Renewable energy data for the United Kingdom

Furthermore, 2022 renewable energy saw an increase of 11% (13.8 TWh) to a record 134.3 TWh while also beating fossil fuels; another first. The increase in the generation was mainly sourced from offshore wind due to increased wind speeds. During 2020, renewable energy accounted for 42.9% of total generation; again another first [11]. During 2021 renewable energy generation decreased by 9.5%, suffering from weather conditions including less wind and rain fall. Although, in the final quarters of 2020 & 2021 the later year saw a 4% increase of which almost half from onshore wind, Figure 1.4 depicts the increase in renewable energy where the largest sector is wind [12].

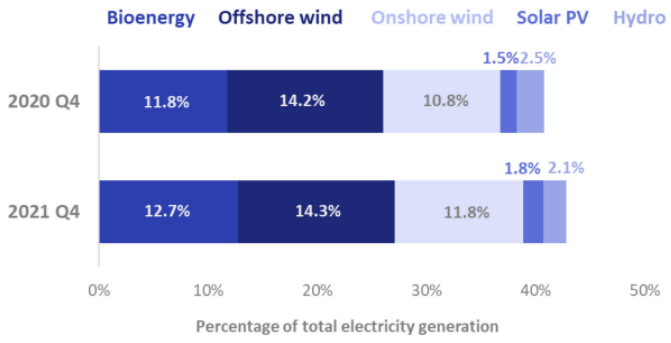

Source: [12]

Figure 1.4: 2021 Renewable energy graph for the United Kingdom

1.1.1 Motivation

The key motivation for this study has been to extend the knowledge of wind turbines and the materials used to manufacture these devices and thus, when fatigued the effect this has on the remaining structure. Developing predictive modelling techniques with the same material will allow the research to develop in terms of visualization of the life cycle of these devices. Thus increasing the positive impact these turbines as a whole have on the environment. An example of these having a negative impact is that it has been estimated that between 5% and 40% of total composite production is scrapped in the UK alone, where in 2010 glass fibre monetary disposal value was £453 million, the main method of disposal currently is land and sea fill [13]. This follows the other motivations for this study; to look into the potential development of biodegradable composites without losing the mechanical attributes. The importance of completing such research will develop work, models, and knowledge on the behaviour of WTBs during normal operating conditions and how these conditions affect the life cycle of these devices. Developing a social understanding that these devices may not be as *renewable* as people may perceive [4].

1.2 Aims & Objectives

The following section outlines the aims & objectives of the project including the hypothesis in which these are set out to successfully or unsuccessfully falsify. The following research hypothesis being proposed:

> *Finite Element and analytic modelling may be used to evaluate the realistic elastic response of quasi-isotropic layered composite material aerodynamic components.*

1.2.1 Aims

- Produce idealized three-dimensional Wind Turbine Blade shells using state-of-the art ANSYS-Spaceclaim direct modelling software and predict their in-service elastic response.
- Perform salient life-cycle predictions of these shell models.
- Produce a body of work worthy of dissemination to the wider scientific community, thereby demonstrating a Mastery of Science in aerodynamic composite material design and simulation.

1.2.2 Objectives

1. Identify candidate designs of medium sized wind turbine blades using reliable literature.
2. Characterize loading conditions for medium sized wind turbine blades.
3. Analyse composite materials used in the construction of wind turbine blades evident in literature.
4. Evaluate the mechanical properties of quasi-isotropic laminate aerospace tokens using Classical Lamination Theory (CLT) and Finite Element (FE) methods.
5. Use verified FE models to predict the life of the aforementioned idealized wind-turbine blades.
6. Critically compare the FE layered shell models with complementary analytic techniques.
7. Critically evaluate the idealized the FE wind-turbine life cycle data with empirical equivalents evident in the literature.
8. Disseminate findings to wider scientific community via the completion of at least one fully refereed Masters of Science thesis.

1.3 Overview of the thesis

The opening chapter to this thesis introduces the topics to be presented throughout the document. Here particular attention is directed towards current wind turbine blade structure which are subsequently modelled. The second chapter of this thesis reviews both classical and up-to-date literature. The major outcome of this section being the identification of previous work, exploring theories and methodologies. The third chapter of the final thesis details theories identified in the former chapter and develops these appropriately. The fourth chapter employs methods, developing: analytical, numerical, and simulation methods. Chapter five of the thesis presents the results from the aforementioned models and methods. Subsequently the results are discussed in the sixth chapter of this thesis. The final chapter begins with a critical reflection on the aims and objectives, stated in the opening chapter; the main scientific conclusions of the work are also developed and any recommendations of further work provided.

1.4 Wind turbine blade anatomy

The information provided herein applies to this research topic, covering areas such as; the design of wind turbine blades, how the shape generates lift, and why this is a key component. Combining the knowledge of why these devices are key to the research along with the initial equations for a greater understanding of the work portrayed throughout this thesis.

1.4.1 Airfoils

The sectional shape of a wind turbine blade is known as an airfoil, a wind turbine airfoil generates aerodynamic lift when in rotation [14]. The anatomy of a 2-Dimensional airfoil contains a number of named areas, Figure 1.5 acknowledges the components of these shapes.

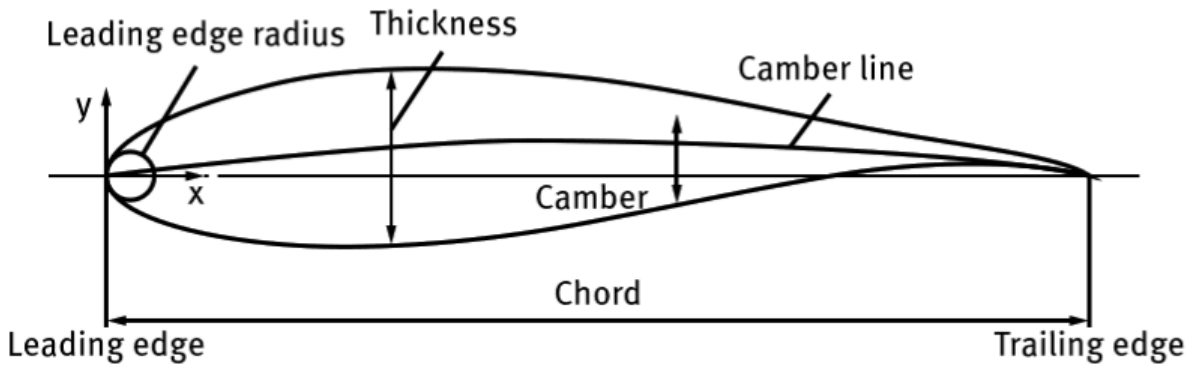

Source: [15]

Figure 1.5: Single element airfoil

When an airfoil is singular, like that in a WTB, it is known as a single element airfoil, compared to an aircraft wing with flaps known as dual or multi element. The leading edge of the airfoil is the furthest forward point, while the the leading edge radius is the radius within; the trailing edge is the furthest rear point. *Chord* is defined as the overall length of the airfoil, measuring from the leading edge to the trailing edge. Thickness of the airfoil can be defined as a percentage of the chord. If the airfoil possessed camber, this is the distance between the straight line along the chord to the mid-point of the thickness, thus making the camber line [15]. Airfoils containing a camber tend to generate more lift and drag, in motorsport applications the wing can be inverted to generate negative lift also known as *downforce* [16]. When not taking into consideration any gravitational, thermal, or any other energy sources the equations for lift and drag are as follows:

$$F_D = \frac{1}{2}\rho u^2 A C_D, \tag{1.1}$$

$$F_L = \frac{1}{2}\rho u^2 A C_L, \tag{1.2}$$

where F_D & F_L are drag and lift forces respectively, ρ is the density of fluid the blade is travelling though, u is the true air speed, A is the area [1], with C_d & C_l being the coefficients of drag and lift respectivly [17]. Furthermore, with this knowledge, the geometry of the blade is not a constant airfoil size and shape over the span but rather a tapering airfoil [18]. Noting Figure 1.6 shows the same two-dimensional airfoil over the span of the blade however it is also with varying chord length. A true representation of a wind turbine blade geometry is multiple airfoils decreasing in chord length over the span of the blade, usually starting at the base as a cylindrical shape [19, 20]. Figure 1.7 shows that down the span of the blade the shape of the airfoil(s) is very different to that of Figure 1.6 while also including the circular base for connection to the hub of the turbine.

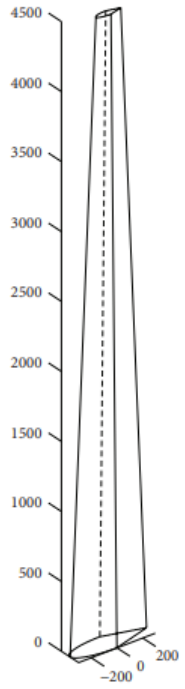

Source: [18]

Figure 1.6: Tapered blade

[1] Span multiplied by the chord length

(a) Cross-sections on 3D blade

(b) Top view of airfoils

Source: [19]

Figure 1.7: True representation of wind turbine blade

Chapter 2

Literature Review

This section of the thesis discusses appropriate literature. Any work done in a similar field to this research will also be explored and reviewed, including those done within the John Tyndall institute (JTi).

2.1 Material properties

Materials within engineering is a vast subject and the selection process can be a critical operation to ensure the structure is successful. Understanding the fundamental principals can involve an understanding of the classification of materials, the properties and how these are affected over time with exposure to the working environment. Advancements in materials have been able to help the development of day-to-day objects, in the 1800s the key materials would of been wood and clay. Advancing to the early 1900s this saw the appearance of plastics, although not widely available until the mid 1900s. Continuing to the modern day, silicon and semiconductors have been developed allowing for electronic devices such as computers and mobile phones to exist [21].

2.1.1 Material characteristics

Within engineering there is a multitude of material types, each with their own advantages and disadvantages when compared. When classifying a material it is dependent on some of the chemical characteristics each material holds. Seven main groups for defining materials are as follows:

1. Metals
2. Ceramics
3. Organic polymers
4. Composites
5. Semi-conductors
6. Biomaterials
7. Advanced materials

Metals are defined by element substances which readily give up electrons. In doing so, these materials form metallic bonds and are capable of conducting electricity. Here, metals can be split into further subsections such, as pure metals, alloyed metals, and ferrous metals.

Ceramics are hardened clay parts in which the material becomes hard, porous, and brittle. These can be used in objects such as pottery and bricks, although more modern uses see them used in gas turbine engines. This type of material can also be broken down into subsections depending on the use.

Organic materials are compounds where carbon is chemically bonded to hydrogen, oxygen, and non-metallic substances. These materials are often naturally occurring such as rubbers and plastics hence the name, organic polymers. These contain subsections further classifying them based on characteristics.

A composite material is defined as a material system containing two or more phases on a macroscopic scale, forming a new material [22]. When making a composite the material properties may be improved [23], such as:

- Strength
- Fatigue
- Mass

- Stiffness
- Corrosion resistance.

Composite materials may be classified depending upon the method in which the material is manufactured, some of the more common types are; particulate, fibrous, and laminated. Where particulate composites contain particles in the matrix, usually suspended within the matrix, the particles can take any shape such as flakes [24]. Fibrous consists of fibres in a matrix, a fibre is defined as material with a high length-to-diameter ratio with a diameter of 5μm to 24μm [25]. While laminated composites are layers of various materials, a minimum of two different materials, usually with noticeable differences in thermal expansion coefficients [23].

Semi-conductors are materials containing electrical properties yet intermediate to conductors and insulators. This classification is sensitive to impurity of atoms, even in minute amounts. These concentrations can be controlled via spatial regions.

Biomaterials are chemically non-toxic and must be compatible with human body tissue, as these are components that are implanted into the human body to replace extensively damaged bone and tissue, caused via trauma or disease.

Advanced materials are reserved for those used within high-technology purposes including military and domestic electronics such as fibre optics or computers. These are usually traditional materials that have been enhanced or developed to increase the capability of the material [26]. Through-out this thesis the focus has been on composites, in particular; glass fibre, as this is the main material used in the construction of wind turbine blades.

2.1.2 Mechanical properties

As each material is classified based upon the chemistry the bonds produce, this changes the property of the material. There is avast amount of properties within each such as, *elasticity, strength, fatigue, hardness,* and *stiffness* [26]. Stress (2.1), strain (2.2), and Young's modulus (2.3) are all linked together while having their own calculations. Strain is showing the elongation compared to its original length, stress is the intensity of force measured by force per unit area, and Young's modulus is the elasticity of the material [27]. The aforementioned equations are as follows:

$$\sigma_i = \frac{F_i}{A_j}, \tag{2.1}$$

$$\epsilon_i = \frac{\Delta L_i}{L_i}, \tag{2.2}$$

$$E_i = \frac{\sigma_i}{\epsilon_i}, \tag{2.3}$$

where the stress (2.1) F_i is the force in the x direction. Here, both i and j are sets from the x, y, and z axis, A is the cross sectional area respective to the applied force, while for strain (2.2), ΔL_i is the change in length in direction x relative to the original length L. Furthermore Poisson's ratio (ν_{ij}) is the linear deformability of a material. This is the contractual transverse strain (ϵ_j) divided by the longitudinal strain (ϵ_i) when displacing in the x direction. The Poisson's ratio of a material can be positive, zero or negative [28, 29], calculated using equation (2.4):

$$\nu_{ij} = -\frac{\epsilon_j}{\epsilon_i} \tag{2.4}$$

modulus of rigidity is the ratio of the shear stress to the shear strain, showing a materials ability to return to its original shape after small amounts of deformation. Shear modulus can be calculated using equation (2.5):

$$G = \frac{\tau_{ij}}{\gamma_{ij}}, \tag{2.5}$$

where τ_{ij} is the shear stress, in a similar notation to that in equation (2.1) and γ_{ij} is the shear strain, similar to equation (2.2).

2.1.3 Material degradation

Materials will naturally degrade over time even when exposed to the designed working environment, such a factor is known as degradation or fatigue. As this research is based upon composite materials, the following fatigue will be in terms of composite materials and how this can be an issue during design. A starting point for fatigue data is understanding the amount of cycles, in this case rotations, the device will experience during it in-service life. Equation (2.6) is a way to calculate the total rotations:

$$N = RL, \tag{2.6}$$

R is the revolutions per minute at the rated wind speed while L is life measured in minutes. This calculation would be able to give an approximate value of rotations during the devices life

at the correct rated wind speed. Understanding the number of rotations or cycles performed by a blade during the life time helps develop the stress-life models otherwise known as $S-N$ curves [30]. These graphs are pictorial examples of the number of cycles, N, compared against the strength, S, these can show how long a device can last under loading conditions, Figure 2.1 is an example of these.

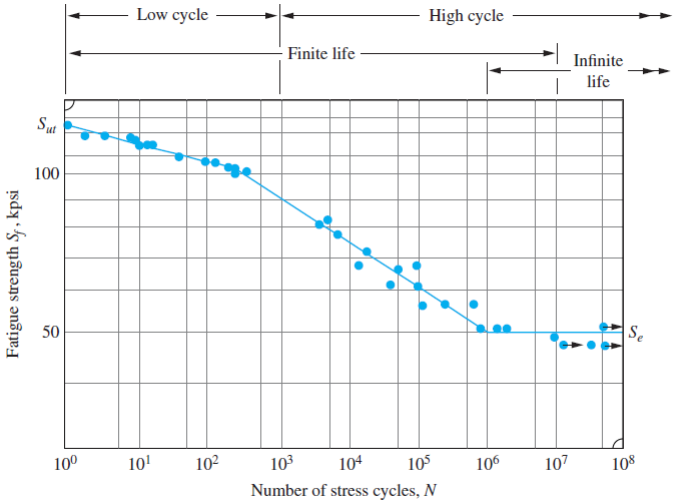

Source: [31]

Figure 2.1: S-N Curve of UNS G41200 Steel

Figure 2.1 shows the number of cycles passes the strength of the material degrades. If the material is not suited for the role, a steep curve will occur whereby more life is being removed from the material resulting in a sooner failure. On the other hand, if the material is over engineered this will extend the life of the material although usually at a financial cost of development. Material degradation is important within the wind energy sector as the blade can be exposed to environments and situations which will be pushing the design envelope to the limit. An example being excessive wind speeds from storms coupled with lightening and moisture damage, all of these may provide additional stresses reducing the overall strength of the material, therefore this may require the blade to be changed before any maintenance is due.

2.2 Composite materials

As previously mentioned the makeup of a composite material is usually carried out in order to develop a material with desirable and advanced properties for the designed use. The use of such matrix materials is the main issue why wind power is not that green. This has been a large focus on the research conducted into this area, aiming to find more green alternatives or new materials called bio-composites. Other research is directed towards the manner in which the material is built and if this can be optimized to ensure desired material properties for specific applications. Examples of research looking into alternative or new materials can be sourced from recent years whereby they explore the feasibility of natural materials such as; hemp, flax, and sisal [32, 33] (known as bio-fibres). The overall results of this research concludes that naturally occurring fibres do exist and can be formed into layers. Although the largest limiting factor of such materials is that some models still rely on commonly used fibres to help reinforce the structure. Without these, the material properties are simply not adequate to be a replacement for carbon and glass fibre types at this current time. Other challenges the new bio-composites have to overcome include cost of manufacture and further development to ensure the properties can allow this type of material to be a true competitor to the more traditional composites [34].

A large amount of research has been conducted into the material properties and how this affects the behaviour of the system when exposed to various situations, measuring the response from the structure. A few instances of this is documented where sections of material taken from a WTB are subjected to testing to a number of standards, the outcome of this research is that the specimens tested did not differ from that expected from literature [35]. The standards used within this research to ensure the experiments were conducted successfully and correctly were as follows:

- ASTM D2344/D2344M-16 [36], testing the short-beam strength of composite materials. Outlining the testing procedure, equipment and its calibrations.
- ASTM D3039/D3039M-14 [37], testing the tensile properties of the composite by outlining the equipment, calibrations and procedure.
- ASTM D6641/D6641M-14 [38], testing for the composites compressing properties via a combined loading compression.
- ASTM D7078/D7078M-12 [39], testing the shear properties of the composite.

Although this area is heavily researched, stand out literature in book form (namely Gibson's Principles of Composite Material Mechanics) are excellent publications stating the

mechanics of the material in a single source, chapters 2 and 7 are the particularly important to this project [40]. The equations seen within this text and the mentioned chapters are key to finding the material properties and the manner in which it is behaving. In a three-dimensional shape, such as a cuboid, the state of stress at a point can be viewed as Figure 2.2 containing 9 stress components σ_{ij} (where x, y, z=1, 2, 3) [40].

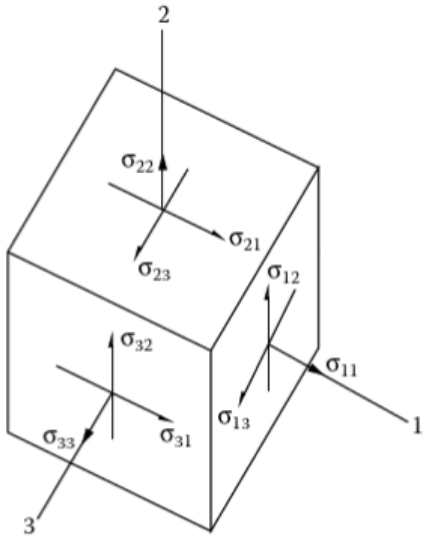

Source: [40]

Figure 2.2: 3-D Stress of a cuboid

Within Figure 2.2 the first subscript references the outward normal of the face which the stress is acting upon, while the second denotes the direction of the stress itself. The deformation at the same point can be described as u_{ij} with corresponding subscripts. There are generally two types of strain resulting from these deformations, *viz.* Within composite there are two types of tensor, continuum strain (ϵ_{ij}) and engineering strain (γ_{ij}) whereby the relationship between these is: $\epsilon_{ij} = \frac{\gamma_{ij}}{2}$ [40]. The relationship between the coordinate axes and the stress components can be calculated by making use of equations of static equilibrium for the wedge-shaped differential element (Figure 2.3), these being the combination of the equations for transformation of stress and strain components from the 12-axes to the xy-axes. If equation (2.7) divided by dA, the the resulting equation is (2.8):

$$\Sigma F_x = \sigma_x dA - \sigma_1 dA \cos^2\theta - \sigma_2 dA \sin^2\theta + 2\tau_{12} dA \sin\theta \cos\theta = 0, \tag{2.7}$$

$$\sigma_x = \sigma_1 \cos^2\theta + \sigma_2 \sin^2 1\theta - 2\tau_{12} \sin\theta \cos\theta. \tag{2.8}$$

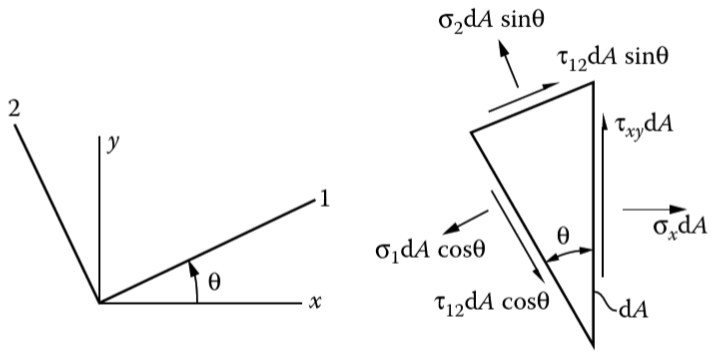

Source: [40]

Figure 2.3: Wedge-shaped differential element

A complete set of transformation equations can developed into matrix form for the stresses in the xy-coordinates. This method is transforming the stresses from the xy-system into the 12 system by using the following matrix; where $c = \cos(\theta)$ & $s = \sin(\theta)$. This can also be done using inverse T to transpose the values from 12 into the xy in equation (2.11):

$$T = \begin{bmatrix} c^2 & s^2 & 2cs \\ s^2 & c^2 & -2cs \\ -cs & cs & c^2 - s^2 \end{bmatrix}, \tag{2.9}$$

$$\begin{bmatrix} \sigma_1 \\ \sigma_2 \\ \tau_{12} \end{bmatrix} = [T] \begin{bmatrix} \sigma_x \\ \sigma_y \\ \tau_{xy} \end{bmatrix}, \tag{2.10}$$

$$\begin{bmatrix} \sigma_x \\ \sigma_y \\ \tau_{xy} \end{bmatrix} = [T]^{-1} \begin{bmatrix} \sigma_1 \\ \sigma_2 \\ \tau_{12} \end{bmatrix}. \tag{2.11}$$

The lamina tensor strains can also be transposed in a similar manner to the stresses by using the T value changing the axis from 12 to xy. Furthermore, the stresses in the xy-plane can be evaluated from the tensor strains via equation (2.12). Where Q is the so-called lamina stiffness matrix, equation (2.13), here $Q^*_{ij} = Q_{ij}$ for all excluding $Q^*_{66} = 2Q_{66}$ this being due to the aforementioned dependency between the continuum strain and engineering

strain tensors. Thus, multiplying these matrices, converting back to engineering strains gives equation (2.14), this result occurs with the use of the Reuters matrix, $[R]$, discussed in the proceeding methods chapter [41]:

$$\begin{bmatrix} \sigma_x \\ \sigma_y \\ \tau_{xy} \end{bmatrix} = [T]^{-1}[Q^*][T] \begin{bmatrix} \epsilon_x \\ \epsilon_y \\ \frac{\gamma_{xy}}{2} \end{bmatrix}, \tag{2.12}$$

$$Q = \begin{bmatrix} Q_{11} & Q_{12} & 0 \\ Q_{21} & Q_{22} & 0 \\ 0 & 0 & 2Q_{66} \end{bmatrix}, \tag{2.13}$$

$$\begin{bmatrix} \sigma_x \\ \sigma_y \\ \tau_{xy} \end{bmatrix} = \begin{bmatrix} \bar{Q}_{11} & \bar{Q}_{12} & \bar{Q}_{16} \\ \bar{Q}_{12} & \bar{Q}_{22} & \bar{Q}_{26} \\ \bar{Q}_{16} & \bar{Q}_{26} & \bar{Q}_{66} \end{bmatrix} [R] \begin{bmatrix} \epsilon_x \\ \epsilon_y \\ \gamma_{xy} \end{bmatrix}, \tag{2.14}$$

where, in (2.14) the $\bar{Q}_{ij}$ are defined as the following equations for the transformed lamina stiffness matrix:

$$\bar{Q}_{11} = Q_{11}c^4 + Q_{22}s^4 + 2(Q_{12} + 2Q_{66})s^2c^2, \tag{2.15}$$

$$\bar{Q}_{12} = (Q_{11} + Q_{22} - 4Q_{66})s^2c^2 + Q_{12}(c^4 + s^4), \tag{2.16}$$

$$\bar{Q}_{22} = Q_{11}s^4 + Q_{22}c^4 + 2(Q_{12} + 2Q_{66})s^2c^2, \tag{2.17}$$

$$\bar{Q}_{16} = (Q_{11} - Q_{12} - 2Q_{66})c^3s - (Q_{11} - Q_{12} - 2Q_{66})cs^3, \tag{2.18}$$

$$\bar{Q}_{26} = (Q_{11} - Q_{12} - 2Q_{66})cs^3 - (Q_{11} - Q_{12} - 2Q_{66})c^3s, \tag{2.19}$$

$$\bar{Q}_{66} = (Q_{11} + Q_{22} - 2Q_{12} - 2Q_{66})s^2c^2 + Q_{66}(s^4 + c^4), \tag{2.20}$$

as seen in equation (2.14), the coordinate system is seen moving from 1's and 2's up to 6. This originates from the stiffness and compliance matrices, C and S respectively, for the materials where for an anisotropic material is as equation (2.21) shows. Here, the principal directions are taken forward for the above calculations, hence C_{66} is carried forward as this

is stiffness in the 12 direction, replacing C_{33} [40]:

$$[C] = \begin{bmatrix} C_{11} & C_{12} & C_{13} & 0 & 0 & 0 \\ C_{12} & C_{22} & C_{23} & 0 & 0 & 0 \\ C_{13} & C_{23} & C_{33} & 0 & 0 & 0 \\ 0 & 0 & 0 & C_{44} & 0 & 0 \\ 0 & 0 & 0 & 0 & C_{55} & 0 \\ 0 & 0 & 0 & 0 & 0 & C_{66} \end{bmatrix}, \tag{2.21}$$

$$[S] = [C]^{-1}. \tag{2.22}$$

2.3 Blade Element Momentum theory

Blade Element Momentum (BEM) theory is currently a widely used method for aerodynamic applications within wind energy generation [42]. The start of this theory was introduced between 1922 and 1925, wherein writings were published stating with the application of elementary physics varying calculations such as mechanical energy can be obtained. The mechanical energy from the air stream when passed through a specified Cross-Sectional Area (CSA) is constrained to a fixed proportion of the energy or power within the air stream [43]. This limit in which the blade can generate mechanical energy from the air stream in known as Betz-Joukowsky Limit with a value of 59.3% [44] based upon the assumption of no friction losses [42, 43]. A summary of work recently carried out looks at the process of BEM and whether there are any alternate methods while comparing and linking these with other methods such as Computational Fluid Dynamics (CFD). Elements of work have been investigating into the theory whereby applying accurate coefficients of lift and drag values (C_L & C_D) in the theory and evaluating the results. Following with discussions about the limitation of BEM being such dimensionless values [45]. Newer sources have suggested that BEM has been developed to overcome these original limitations by the means of empirical corrections from other similar theories namely, helicopter applications. The manner in which these limitations have been overcome is by iteratively improving the theory, an example being for tip loss, original BEM ignores tip loss whereas Prandtl proposed that it could be corrected via modelling the wake with vortex sheets [46, 47]. Looking into the future of BEM theory, it is a method that still relies on the inputted data, therefore if incorrect or misleading data is used the results will be affected. Some research suggests that an alternative to BEM named Actuator Line (AL) model could be a replacement for the theory, as it contains aspects such as wake [48]. Although a recent study developed a simple method of calculating BEM using

a single equation and input, this greatly reduces the time in order to have the equations converge. Equation (2.23) demonstrates this reduced method to the theory:

$$f(\Phi) = \frac{sin\Phi}{1-a} - \frac{cos\Phi}{\lambda_r(1+a')} \tag{2.23}$$

where Φ is the local inflow angle, a is axial induction factor, λ_r is local tip speed ratio, and a' is tangential induction factor. BEM theory provides a strong foundation into the research of this project in order to develop methods into results.

2.4 Finite Element Analysis

Finite Element Analysis (FEA) allows for the simulation and modelling of physical phenomena by using algebraic, differential or integral equations. An example being Ordinary Differential Equations (ODE) & Partial Differential Equations (PDE) [49] referred to as Finite Element Method (FEM). Static structural simulations is a form of FEA as these develop results by using ODEs and PDEs of a structure, a wind turbine blade being an example of such. Recent research in this area has used any number of different approaches to developing this type of analysis to gain knowledge on the behaviour of blades. FEA has been employed since the 1950's with the structural analysis of aircraft [50]. Each element of the FEA adheres to:

$$k_i = h \iiint_V \overrightarrow{B}^T [D] \overrightarrow{B} \, d_V \tag{2.24}$$

where k is the stiffness matrix, $[D]$ is the elastic coupling, and B is the gradient of the shape function. In-order to evaluate the global stiffness matrix, relating the nodal displacements to the forces applied; equation (2.24) will be utilized and imposing shell formulations, equation (2.25) is formed:

$$k_i = h \iint_{Ai} \overrightarrow{B}^T [D] \overrightarrow{B} \, d_A \tag{2.25}$$

where h is the shells thickness and $[A]$ being a sparse matrix comprised of zeros and ones. The shape functions within ANSYS are presented as:

$$u = \frac{1}{4}(u_1(1-\xi)(1-\eta) + u_2(1+\xi)(1-\eta) + u_3(1+\xi)(1+\eta) + u_4(1-\xi)(1+\eta)) \tag{2.26}$$

with u being the translation within direction ξ [51].

A 2018 study progressed the detail and fidelity of FEA studies by developing the geometry using a novel parametric block method where each block has its own configurations. This approach allowed the full blade to be modelled with high accuracy, an example being that one of the blocks used to model the blade could be a single or opposing panel capable of making a single face from a panel. This panel later meshed with shell elements or creates a cell later meshed with solid elements. Throughout the modelling of this blade eighteen different blocks are used, the results of this modelling approach allows for much more detail to be drawn into the model, resulting in more accurate results and data [52].

2.5 Similar Work in this area

The JTi has work in a similar area to the content of this paper, a number of previous studies performed by Dr Whitty and Mr Walsh in partnership with Prof Henderson, on the behaviour of wind turbine blades. The research began with Dr Whitty looking at the design process of aerodynamic components with specific attention paid towards wind turbine blades, this research involved the modelling of a 4.2m National Advisory Committee for Aeronautics (NACA) 63-621 tapering blade to find the strain field of the device, as this had been identified as an area for failure throughout other literature. The conclusions of this paper show that in all cases tested a stiffening rib was required to meet the 10% displacement design criteria although the models tested did not fail at the root leading to the understanding that the models were not fully optimized in a structural manner [18]. The further work discussed researching into variations of composite material lay-ups, this being an objective of this work. Furthermore, the research conducted within the institute also created a review paper of various loading conditions placed on a blade, both with and without a stiffening structure down the centre (a stiffening web). The conclusions of this paper found that an asymmetric blade reduced the second moment of area from $20.5 - 24$ million mm^4 in a symmetrical blade to $9.5 - 12$ million mm^4, this is a reduction in $51\% - 55\%$. In order to develop a full comprehensive review, a various amount of loading conditions had to be considered, some for example being Uniformly Distributed Load (UDL), Bernoulli Dynamic Distributed Load (BDDL), and Quadratically Distributed Load (QDL). While producing a vast amount of data for blades with and without the stiffening web all under different loading conditions. The paper also takes into account whether the blade is static or dynamic, where in each case a realistic load was determined. As for the dynamic blade this was the BDDL equation while static was Bernoulli Stationary Distributed Load (BSDL) [53]. However, the research into wind turbine blades is still continuing within the group, currently Mr Walsh of BAE Systems

and Dr Whitty are collaborating developing models for wind turbine blades where NACA 2414 & 2415 have been selected to form the airfoil profile for these devices. Mr Walsh's work within JTi made advancements on Dr Whitty's work by utilizing the aforementioned NACA profiles to form the shape of these WTBs which would then be used for analytical simulations and numerical calculations to develop the research. As this work is a continuation of these pieces some of the data will be used; namely, NACA profiles, chord length, and blade span.

Composite material fatigue has been subject to areas of research of recent where the main aim has been to develop sound engineering theories of how such materials fatigue and methods to improve fatigue resistance. One area is regarding the material properties or make-up itself with research looking into how the volume fractions, lay-up sequences, and fibre materials affect how the material behaves during loading to cause fatigue. The main conclusions of this work indicate that the location of failure points can vary between the matrix, fibre, and where these interact; yet is more common when in the longitudinal axis of the fibre as cracks are allowed to propagate further along the fibre [54], suggesting that fibre orientation can have an impact. Furthermore, fibre orientation research has developed work with results conveying that the method of building a layup sequence will affect the overall materials' ability to withstand cyclic loading. The application of varying layup sequences exhibits higher fatigue resistance when these have more complex orientation methods; using right-angle layups ($[0, 90]$) tends to fail earlier when compared to others such as $[-45, 0, 45, 90]$, this happens due to more fibres in altering directions help with structural integrity. This result is additionally highlighted by finding that Young's modulus and Poisson's ratio are significantly different for out of fibre direction loading [55]. Continual development of composite materials to improve fatigue properties has involved the inclusion of additional fibres, changing the terminology of the material to a hybrid composite containing a mixture of carbon and glass fibres within an epoxy resin. The conclusion of this work found that whilst the addition of carbon to a typical glass fibre does improve the fatigue response, this is still marginal [56]. The general trend of work in this area has been developing models, methods, and theories in order to better calculate fatigue within the material and how these can be improved, although the idea of developing new materials to have improved properties is seldom present for this size of turbine blade (< 5m).

Wind turbine blade modelling is a subject that has seen research activities; the main content here is how the structure fatigues and methods of reducing such an event. A second stage of fibre orientation studies determined the effect this has on the device in question. The main results have shown that the orientation of the fibres within the construction of wind turbine blades is vital to performance under loading conditions; $[0, 90]$ sequences would

experience rapid deterioration for maximum stress within the 45° due to a decrease in the Poisson's ratio and tensile characteristics. However, when using the $[-45, 0, 45, 90]$ layup sequence the rate of deterioration of the material significantly improved, although it is noticed that adding more plys will increase the total mass of the blade; thus the orientation of the fibres to maximise fatigue resistance is paramount [55]. This result has been additionally verified during other studies where fibre orientation has been shown to affect the performance of the blade while also investigating the location and method of fatigue. Resulting in the observation of fatigue propagation beginning at the matrix material. Although in areas of the turbine blade such as the leading edge, it has been found that fatigue can start at the fibre [57], leading on from a previous study estimating the fatigue life of the device to be more than 20 years [58]. The average life of wind turbine blades is another area of research focus, attempting to extend the life by developing new materials such as basalt fibre. These new materials show better overall mechanical properties including a Young's modulus value 2.5 times larger than glass fibre, although this advancement only transforms into a fatigue benefit when utilized within larger blade structures; typically 50 metres or larger. Whilst using the new material on larger blades it is exhibiting a life of 29 years, whereas comparing that to a typical glass fibre blade would see a life of less than 1 year. A secondary result of this is providing an alternative material to typical glass fibre which could improve the fatigue properties of these devices [59].

Chapter 3

Theory

This section will detail the theory developed from knowledge gained in literature, this will be an expanse on the equations, nomenclature and understanding further employed within the methods used. The areas discussed are specific to the work carried out and that will be applied.

3.1 Theory of bending

In order to develop a rigorous model for the WTB, it is key to grasp how the model can be seen as a cantilever beam with a load applied to it. The loading condition applied to this beam is known as a Uniformly Distributed Load (UDL) here the load is applied evenly over the length of the beam or with reference to the blade this is the span. Figure 3.1 shows how this appears on the cantilever beam along with equation (3.1) show the calculation used to return the amount of displacement from the blade or beam in terms of x.

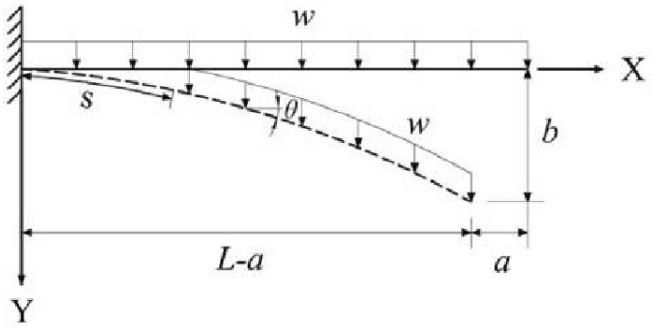

Figure 3.1: Uniformly Distributed Load

$$y = \frac{\omega x^2}{24EI}(x^2 + 6l^2 - 4lx) \tag{3.1}$$

where ω is the uniformly distributed load on the beam, x is the neutral axis of the beam, E is the Youngs modulus of the beam, I is the second moment of are with l being the length of the beam. In this case parallel axis theorem has been used to calculate the second moment of area for the wing, this is the practice of taking the second moment of area from an axis parallel to that of the second moment of area axis. To calculate the second moment of area around the parallel axis equation (3.6) is used:

$$I_{xx} = \int (y + h)^2 dA \tag{3.2}$$

thus:

$$I_{xx} = \int y^2 dA + 2h \int y dA + h^2 \int dA \tag{3.3}$$

from equation (3.3) we can see that the first integral is that of the second moment of area $\int y^2 dA$ [60]. Therefore the second and third integral are equations (3.4) & (3.5) whilst $\bar{y} = 0$:

$$\int y dA = A\bar{y} = 0, \tag{3.4}$$

$$h^2 A, \tag{3.5}$$

resulting in:

$$I_{xx} = I_x + h^2 A. \tag{3.6}$$

The main uses for equation (3.6) within this research are to calculate the bend of the beam when subjected to a UDL to assess the more rigid blade between those chosen.

3.1.1 Euler-Bernoulli Beam Theory (EBT)

This theory developed around 1750 is a model of how beams behave under bending and axial forces. EBT relies on a number of assumptions in order to work, firstly that of plane sections remain in plane under bending. In these examples, the displacements are u, v, w along the coordinates x, y, z:

$$u(x, z) = -z\frac{dw_0}{dx}, \tag{3.7}$$

$$w(x, z) = w_0(x), \tag{3.8}$$

where w_0 is the transverse deflection of $(x, 0)$ along the mid-plane where z is zero. Equations (3.7) and (3.8) suggest that before and during the deformation that straight lines normal to the mid-plane will remain normal [61] as seen in Figure 3.2.

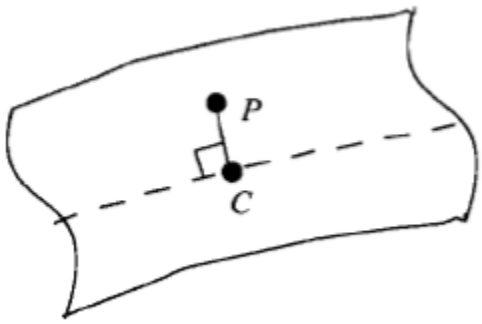

Source: [62]

Figure 3.2: Euler-Bernoulli assumption

As a result of this assumption, both transverse shear and normal strains are neglected. Furthermore, the second assumption made in this theory is that if deformed angles of the beam are small then it can aid the analysis, where by equation (3.9) is defined:

$$\theta = \frac{du_y(z)}{dz} \tag{3.9}$$

where $du_y(z)$ is the change in location in comparison the the neural axis z. If the slope of the beam is considered to be small this would be assumed zero. The main equation within EBT is that of equation (3.10):

$$\frac{d^2u_y(z)}{dz^2} = \frac{M}{EI} \tag{3.10}$$

where M is the bending moment acting on the beam, I being the second moment of area of the beam cross section with the first fraction being the second derivation of the deflection, equation (3.9) [63]. The analytical method mentioned builds from the basis of beam mechanics where the foundation equation is defined as (3.11):

$$\frac{M}{I} = \frac{\sigma}{y} = \frac{E}{R}, \tag{3.11}$$

where σ is the stress on a layer being a distance, y, from the neutral axis. In the third fraction, E is the modulus of elasticity, while R is the beam radius of curvature [64]. Taking equation (3.11), equation (3.13) is an algebraic relationship that can solve the displacement field [18, 53]:

$$\frac{d^2u_y(z)}{dz^2} = \frac{M(x,z)}{EI}, \tag{3.12}$$

thus:

$$\epsilon_z = \frac{M(z)y(x,z)}{EI(x,z)}. \tag{3.13}$$

3.1.2 Timoshenko Beam Theory (TBT)

In the TBT model cross-section will remain rigid on your plane similar to EBT, however, unlike that of EBT plane sections do not remain normal under bending, as seen in Figure 3.3. Also, this theory can take into account rotation as per equation (3.14). Due to taking rotation into account, this make TBT a less stiff model when compared with EBT as this rotation seen as shear deformation:

$$u(x,z) = z\phi(x) \tag{3.14}$$

where these are the same as in equations (3.7) and (3.8), with ϕ is the rotation of the cross section [61]. Here equation (3.8) is also used, remaining the same from EBT. Furthermore to the displacement fields, the strain-displacement relations are given as:

$$\epsilon_{xx} = \frac{\partial u}{\partial x} = z\frac{d\phi}{dx}, \tag{3.15}$$

$$\gamma_{xz} = \frac{\partial u}{\partial z} + \frac{\partial \omega}{\partial x} = \phi + \frac{d\omega_0}{dx}, \tag{3.16}$$

with the transverse shear strain being nonzero [61]. The stress within this model are determined by:

$$\sigma_{yy} = E\epsilon_{yy}, \tag{3.17}$$

$$\sigma_{xy} = kG(\phi_z + \frac{\partial u_x}{\partial y}), \tag{3.18}$$

$$\sigma_{yz} = kG(\phi_x + \frac{\partial u_z}{\partial y}), \tag{3.19}$$

where k is the shear correction factor and G is the shear modulus found in equation (2.5). The shear predicted by the shear requires the correction as this model yields a constant value above the cross-section whereby it is parabolic in order to allow the unloaded edges of the cross section to remain stress-free [65]. The stress resultants are calculated by integration of the axial stress cross section:

$$N = \int_{\Omega} \sigma_{yy} d\Omega, \tag{3.20}$$

$$M_x = -\int_{\Omega} \sigma_{yy} z d\Omega, \tag{3.21}$$

$$V_x = \int_{\Omega} \sigma_{xy} d\Omega, \tag{3.22}$$

where N is the axial force, M_x is bending moment against the x axis and V_x is the shear force along the x axis; Ω is the beam cross-section with planes orthogonal to the axis [65].

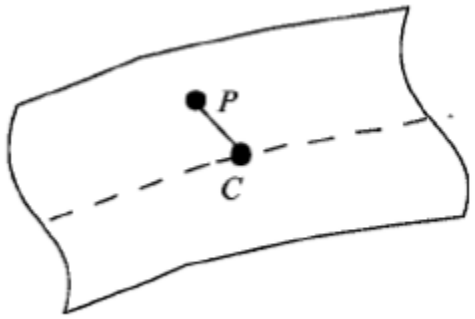

Source: [62]

Figure 3.3: Timoshenko assumption

3.1.3 Castigliano's theorem

Castigliano's theorem came around as an Italian engineer named Alberto Castigliano employed Betti's reciprocal theorem and created a formula for linearly elastic structures [31]. Although this theorem is not directly related to bending theories it can be applied to calculate maximum displacement of a beam under load. The equation from the theorem is:

$$\frac{\partial U}{\partial P_i} = \delta_i \tag{3.23}$$

where the partial derivative of the strain energy is U, with respect to the external load, P. The deflection is δ_i. However, when the external load is a bending moment or torque the equation changes to the following equation (3.24):

$$\frac{\partial U}{\partial C_i} = \theta_i \tag{3.24}$$

here, the C_i is the bending moment or the torque while θ_i is the slope or angle of twist associated with the applied moment [31]. To apply this to the bending moment of the tapered blade the following has to be applied:

$$y = \int_0^L \frac{M(z)}{EI(z)} M_P(z) dz \tag{3.25}$$

where $M(z)$ is the bending moment, $EI(z)$ is the Young's modulus of the material multiplied by the second moment of the blade found by using an average of the chord lengths while $M_P(z)$ is the fictitious moment at the bend of the blade, hence the reasoning for allowing $M_P(z)$ to be equal to $-z$. The primary aim of including this theory into the work is to verify that of the bending from numerical and analytical experiments.

3.2 Classical Lamination Theory

The $\bar{Q}_{ij}$ matrix in equation (2.14) can be used to calculate the A_{ij}, B_{ij} and D_{ij} matrices. Matrix A, (3.26), is the *in-plane stiffness matrix*, these terms are related to normal stresses and strain except for terms A_{16} and A_{26} as these represent normal strains to shear stresses and shear strains to normal stresses. Matrix D, (3.29), is *flexural stiffness matrix* and displays the amount of curvatures in the plate with bending moments. Matrix B, (3.27) and (3.28), is the coupling matrix between A and D named *coupling matrix*, terms B_{16} and B_{26} relate twisting strains with normal stresses and shear strains with bending stresses [66]. When B is equal to 0 this indicates that the laminate is symmetrical. The B matrix can consist of two matrices resulting in identical answers as shown in equation (3.30), thus being condensed to equation (3.31)

$$\begin{bmatrix} N_x \\ N_y \\ N_{xy} \end{bmatrix} = \begin{bmatrix} A_{11} & A_{12} & A_{16} \\ A_{12} & A_{22} & A_{26} \\ A_{16} & A_{26} & A_{66} \end{bmatrix} \begin{bmatrix} {\epsilon_x}^0 \\ {\epsilon_y}^0 \\ {\gamma_{xy}}^0 \end{bmatrix} \tag{3.26}$$

$$\begin{bmatrix} N_x \\ N_y \\ N_{xy} \end{bmatrix} = \begin{bmatrix} B_{11} & B_{12} & B_{16} \\ B_{12} & B_{22} & B_{26} \\ B_{16} & B_{26} & B_{66} \end{bmatrix} \begin{bmatrix} {\epsilon_x}^0 \\ {\epsilon_y}^0 \\ {\gamma_{xy}}^0 \end{bmatrix} \tag{3.27}$$

$$\begin{bmatrix} M_x \\ M_y \\ M_{xy} \end{bmatrix} = \begin{bmatrix} B_{11} & B_{12} & B_{16} \\ B_{12} & B_{22} & B_{26} \\ B_{16} & B_{26} & B_{66} \end{bmatrix} \begin{bmatrix} k_x \\ k_y \\ k_{xy} \end{bmatrix} \tag{3.28}$$

$$\begin{bmatrix} M_x \\ M_y \\ M_{xy} \end{bmatrix} = \begin{bmatrix} D_{11} & D_{12} & D_{16} \\ D_{12} & D_{22} & D_{26} \\ D_{16} & D_{26} & D_{66} \end{bmatrix} \begin{bmatrix} k_x \\ k_y \\ k_{xy} \end{bmatrix} \tag{3.29}$$

$$\begin{bmatrix} N_x \\ N_y \\ N_{xy} \\ M_x \\ M_y \\ M_{xy} \end{bmatrix} = \begin{bmatrix} A_{11} & A_{12} & A_{16} & B_{11} & B_{12} & B_{16} \\ A_{12} & A_{22} & A_{26} & B_{12} & B_{22} & B_{26} \\ A_{16} & A_{26} & A_{66} & B_{16} & B_{26} & B_{66} \\ B_{11} & B_{12} & B_{16} & D_{11} & D_{12} & D_{16} \\ B_{12} & B_{22} & B_{26} & D_{12} & D_{22} & D_{26} \\ B_{16} & B_{26} & B_{66} & D_{16} & D_{26} & D_{66} \end{bmatrix} \begin{bmatrix} {\epsilon_x}^0 \\ {\epsilon_y}^0 \\ {\gamma_{xy}}^0 \\ k_x \\ k_y \\ k_{xy} \end{bmatrix} \tag{3.30}$$

$$\begin{bmatrix} N \\ M \end{bmatrix} = \begin{bmatrix} A & B \\ B & D \end{bmatrix} \begin{bmatrix} \epsilon^0 \\ k \end{bmatrix} \tag{3.31}$$

wherein:

$$A_{ij} = \int_{\frac{-t}{2}}^{\frac{t}{2}} (\bar{Q}_{ij})_k dz = \sum_{k=1}^{n} (\bar{Q}_{ij})_k (z_k - z_{k-1}) \tag{3.32}$$

$$B_{ij} = \int_{\frac{-t}{2}}^{\frac{t}{2}} (\bar{Q}_{ij})_k dz = \frac{1}{2} \sum_{k=1}^{n} (\bar{Q}_{ij})_k (z_k^2 - z_{k-1}^2) \tag{3.33}$$

$$D_{ij} = \int_{\frac{-t}{2}}^{\frac{t}{2}} (\bar{Q}_{ij})_k dz = \frac{1}{3} \sum_{k=1}^{n} (\bar{Q}_{ij})_k (z_k^3 - z_{k-1}^3) \tag{3.34}$$

where t is the thickness of the laminate, k is the kth lamina, while z_{k-1} and z_k are the distances the the kth lamina shown in Figure 3.4; n in the matrix is the total number of laminate. The N matrix is the in-plain forces per unit length, while M is the moments per unit length. The resulting matrices of equation (3.31) contain ϵ^0 as the mid-plane strains, while k is the curvature of the composite when subjected to strain.

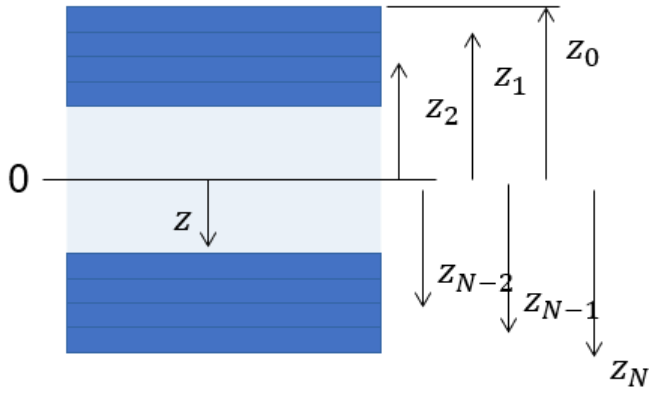

Source: [40]

Figure 3.4: kth lamina

Utalizing the above matrices the following will be used for Young's modulus of the composite for longitudinal, transverse and flexural:

$$E_x = \frac{1}{tA'_{11}}, \tag{3.35}$$

$$E_y = \frac{1}{tA'_{22}}, \tag{3.36}$$

$$E_{fx} = \frac{12}{t^3 D'_{11}}, \tag{3.37}$$

$$E_{fy} = \frac{12}{t^3 D'_{22}}, \tag{3.38}$$

where the A % D are from the A and D matrices although inverse and t is the total thickness of the composite material. Here it is also important to note the manner in which the Poission's ratio for the composite is calculated:

$$\nu = -\frac{A'_{12}}{A'_{11}} \tag{3.39}$$

where both of the values taken are from the resulting A matrix yet, its inverse.

3.3 Numerical solutions

As part of this research there are some numerical solutions that are a key part of the theory in order to develop methods. In this section the two main theories seen in literature and used within the methods of this research are that of the Runge-Kutta and FEA. This section will be presenting the equations within each of the theories and how these are calculated for later reference within the methods of this research.

3.3.1 Runge-Kutta techniques

During the mathematical modelling of the wind turbine blade ODEs can be present, in some cases these do not necessary have analytical solutions, where by numerical models such as Runge-Kutta becomes key. The starting point of this theory is the the solution to a generic problem and compare this with a series produced by a numerical scheme of which contains unspecified parameters. The two series are then forced to agree for as many terms as possible in the expansion [67]. To start with the original differential equation is integrated

$$\frac{dy}{dt} = f(t,y) \rightarrow y(t) = \int_0^t f(t,y)dt \tag{3.40}$$

therefore

$$y_{n+1} = \int_0^{t_n} f(t,y)dt + \int_{t_n}^{t_{n+1}} f(t,y)dt \tag{3.41}$$

essentially changing the task from differentiation to integration, doing this the second order Taylor series needs to be expanded around the midpoint

$$f(t,y) \approx f(t_{n+1/2}, y_{n+1/2}) + (t - t_{n+1/2})\frac{df}{dt} \tag{3.42}$$

when evaluated around the midpoint, the second term of equation (3.42) disappears. This leaves the following:

$$f(t,y) \simeq f(t_{n+1/2}, y_{n+1/2}) \rightarrow y_{n+1} \simeq y_n + hf(t_{n+1/2}, y_{n+1/2}) \tag{3.43}$$

although, at this stage it cannot yet be applied as $y_{n+1/2}$ is unknown therefore, this is approximately calculated as:

$$y_{n+1/2} \simeq y_n + \frac{dy}{dt}(\frac{h}{2}) \simeq y_n + \frac{1}{2}hf(t_n, y_n). \tag{3.44}$$

Therefore, in the fourth order Runge-Kutta method requires four gradients to calculate y_{n+1} [68]:

$$y_{n+1} = y_n + (K_1 + 2k_2 + 2K_3 + K_4)/6 \tag{3.45}$$

where:

$$K_1 = hf(t_n, y_n), \tag{3.46}$$

$$K_2 = hf(t_n + h/2, y_n + K_1/2), \tag{3.47}$$

$$K_3 = hf(t_n + h/2, y_n + K_2/2), \tag{3.48}$$

$$K_4 = hf(t_n + h, y_n + K_3), \tag{3.49}$$

these will be used through this research in aiding the solving of ODEs.

3.3.2 Finite Element Analysis

As part of this research involves simulations using software such as ANSYS Workbench and APDL, the calculations used within these software can depend on how these are modelled. An example of modelling within this work uses an element named 'shell elements', these are making the structure out of plates acting as a curved surface by forming a middle surface. Although, when an external force is applied to a shell structure the stress resultants of the middle surface will now have tangential and normal components [69]. Figure 3.5 shows a typical shell element with the external faces curved, while the sections across the thickness is generated by straight lines.

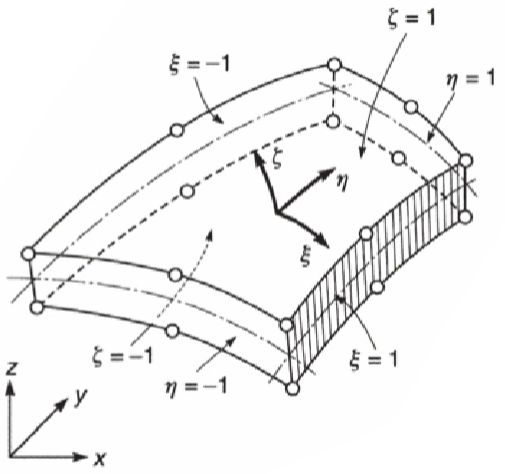

Source: [69]

Figure 3.5: General shell element

Here, the equation for the relationship between the Cartesian coordinates and the curvilinear coordinates take the from of:

$$\begin{Bmatrix} x \\ y \\ z \end{Bmatrix} = \sum N_a(\xi,\eta) \left(\frac{1+\zeta}{2} \begin{Bmatrix} \bar{x}_a \\ \bar{y}_a \\ \bar{z}_a \end{Bmatrix}_{top} + \frac{1-\zeta}{2} \begin{Bmatrix} \bar{x}_a \\ \bar{y}_a \\ \bar{z}_a \end{Bmatrix}_{bottom} \right) \tag{3.50}$$

where ξ & η are the curvilinear coordinates in the mid surface while ζ is the linear coordinate for the thickness. Pairs of nodal points such as $\bar{x}_{a_{top}}$ & $\bar{x}_{a_{bottom}}$ are Cartesian coordinates describing the shape of the element. Equation (3.50) assumes that ξ, η, and ζ vary between -1 and 1 on the respected faces forming a relationship of both sets of coordinates. For Figure 4.2, $N_a(\xi,\eta)$ is a standard two-dimensional shape function at the top and bottom of nodes a and zero at all others, while taking the value of unity. Now, the the relationship can be rewritten as:

$$\begin{Bmatrix} x \\ y \\ z \end{Bmatrix} = \sum N_a(\xi,\eta) \left(\begin{Bmatrix} \bar{x}_a \\ \bar{y}_a \\ \bar{z}_a \end{Bmatrix} + \frac{1}{2}\zeta V_{3a} \right) \tag{3.51}$$

where:

$$\begin{Bmatrix} \bar{x}_a \\ \bar{y}_a \\ \bar{z}_a \end{Bmatrix} = \frac{1}{2}\left(\begin{Bmatrix} \bar{x}_a \\ \bar{y}_a \\ \bar{z}_a \end{Bmatrix}_{top} + \begin{Bmatrix} \bar{x}_a \\ \bar{y}_a \\ \bar{z}_a \end{Bmatrix}_{bottom} \right) \tag{3.52}$$

and

$$V_{3a} = \begin{Bmatrix} \bar{x}_a \\ \bar{y}_a \\ \bar{z}_a \end{Bmatrix}_{top} - \begin{Bmatrix} \bar{x}_a \\ \bar{y}_a \\ \bar{z}_a \end{Bmatrix}_{bottom} . \tag{3.53}$$

This now means x_a represents the mid-surface nodal coordinates while V_{3a} is a vector whose length is the shell director and is the length of the shell thickness. The displacement of the element takes a similar form to that of equation (3.53), as per equation (3.54):

$$\begin{Bmatrix} u \\ v \\ w \end{Bmatrix} = \sum_a N_a(\xi, \eta) \left(\begin{Bmatrix} \bar{u}_a \\ \bar{v}_a \\ \bar{w}_a \end{Bmatrix} + \frac{1}{2}\zeta t_a [v_{1a} - v_{2a}] \begin{Bmatrix} \bar{\alpha}_a \\ \bar{\beta}_a \end{Bmatrix} \right) \tag{3.54}$$

where t_a is the shell thickness at node a and the corresponding rotations, $\bar{\alpha}_a$ and $\bar{\beta}_a$. The displacement in the element is taken to be uniquely defined by the Cartesian components of the mid-surface node displacement, these two directions are denoted as v_{1a} and v_{2a}. The similarity can be seen through Figure 3.6.

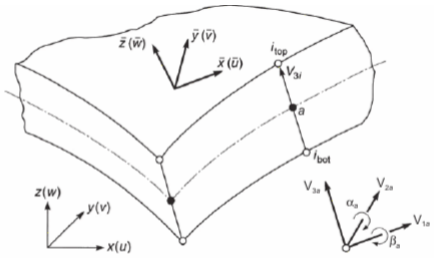

Source: [69]

Figure 3.6: Shell element displacements

Furthermore to the shell element type, the definition of stresses and strains within the element are in the directions of orthogonal axes in relation to the surface and this is essential if taking account for the basic shell assumptions. In this case, if at any point a normal $\bar{z}$ along with the other two orthogonal axes $\bar{x}$ and $\bar{y}$ then the strain components give the

three-dimensional relationship:

$$\bar{\epsilon} = \begin{bmatrix} \epsilon_{\bar{x}} \\ \epsilon_{\bar{y}} \\ \gamma_{\bar{x}\bar{y}} \\ \gamma_{\bar{y}\bar{z}} \\ \gamma_{\bar{z}\bar{x}} \end{bmatrix} \tag{3.55}$$

with direction $\bar{z}$ strain is neglected, note that none of these directions coincide with curvilinear coordinates, however, $\bar{x}$ and $\bar{y}$ are in the plane $\xi\eta$. the stresses for these corrisponding strains are that of:

$$\bar{\sigma} = \begin{bmatrix} \sigma_{\bar{x}} \\ \sigma_{\bar{y}} \\ \tau_{\bar{x}\bar{y}} \\ \tau_{\bar{y}\bar{z}} \\ \tau_{\bar{z}\bar{x}} \end{bmatrix} = \bar{D}(\bar{\epsilon} - \bar{\epsilon}_0) + \bar{\sigma}_0 \tag{3.56}$$

where, $\bar{\epsilon}_0$ and $\bar{\sigma}_0$ are initial strains and stresses and $\bar{D}$ is usually the elasticity matrix, thus linking to the material properties used within the simulations [70].

3.4 Degradation/Fatigue

Fatigue of a material is the measurement of how much strength remains of a material over time due to loading throughout the devices life, ultimately damage caused by fatigue can start as a crack on a macroscopic level. When unnoticed this will begin to grow with each load and eventually leading to fatigue failure whereby the device is destroyed [71].

> *Components subjected to repeated loading may break even at load levels so low that the stress in the material are far below the tensile strength or even the yield limit of the material. This type of failure is called fatigue. Although the fatigue phenomenon has been known for over 150 years, material fatigue is still very common. It is considered that some 60 to 90 percent (depending on how fatigue is defined and which components that are considered) of all mechanical failures are due to fatigue* [72].

Some devices such as wind turbines may be subjected to sinusoidal periodical patterns as these are in rotation, due to this the cycle tends to exhibit maximum and minimum stresses ($\sigma_{max}\&\sigma_{min}$) leading to a mean stress σ_m and an amplitude stress σ_a.

$$\sigma_m = \frac{(\sigma_{max} + \sigma_{min})}{2} \tag{3.57}$$

and

$$\sigma_a = \frac{(\sigma_{max} - \sigma_{min})}{2} \tag{3.58}$$

furthermore to these equations, these are incorporated into some fatigue models where plotting σ_a against σ_m. At zero mean stress, the amplitude becomes the endurance limit σ_e. While σ_m increases the point of failure will be lower than that of the endurance limit as the amplitude decreases. Yielding happens when the yield stress of the material is lower compared to the mean stress, connecting a line on a graph between yield stress and endurance limit in known as the Soderberg line, seen in Figure 3.7. Alternatively, using the materials ultimate stress in place of the yield is known as the Modified Goodman line.

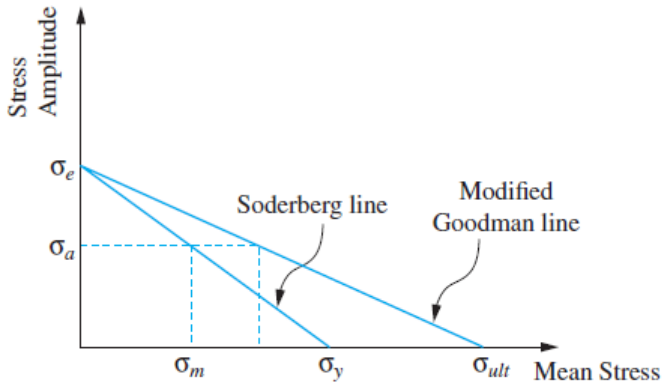

Source: [31]

Figure 3.7: Stress amplitude with mean stress

Over time, the material will degrade with each cycle, as mentioned in §2, S-N graphs are a method of plotting residual strength of a material in comparison to the number of cycles performed by the device Figure 2.1 shows an example graph. The calculation related to the S-N graphs is as below:

$$S^m N_f = K, \tag{3.59}$$

where S is failure strength of the material after N_f cycles, m is termed the fatigue index and K is the fatigue strength coefficient. These values can be used in a FEA package to assess how the material will fatigue over time. Another example of calculating the fatigue values of the device can be done through equation (3.60):

$$S = A\log(N_f) + B, \tag{3.60}$$

where the same as equation (3.59) applies for S and N_f while A and B are parameters related to the materials; in a similar manner to K and m. Figure 3.8 depicts the generic S-N curve for composite and aluminium materials; here, σ_{rupture} is the stress present in the material during failure, akin to that of the fatigue limit which has been assumed in this work [73]. Figure 3.8a shows a generic fatigue graph for a composite material, whilst Figure 3.8b shows a comparison to a generic Aluminium alloy.

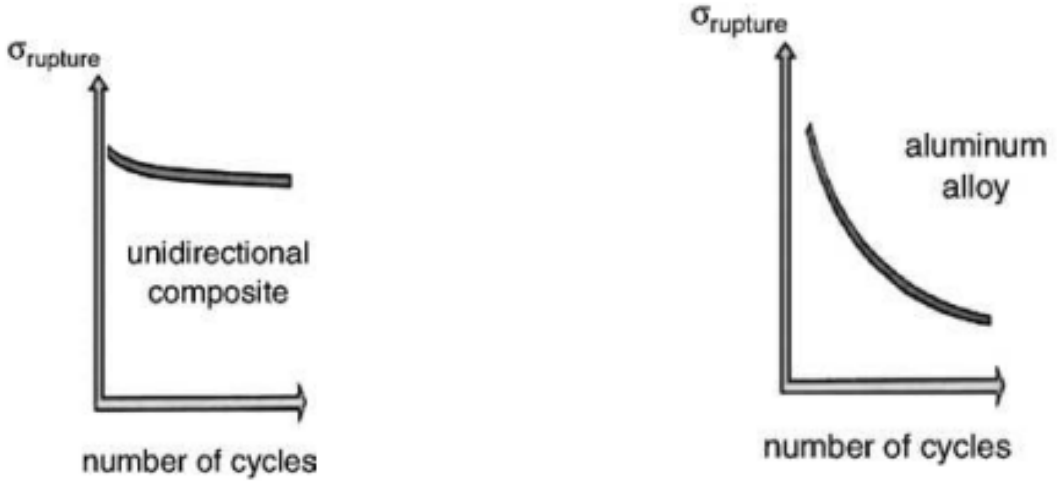

(a) Composite

(b) Aluminium alloy

Source: [74]

Figure 3.8: Generic composite & Aluminium alloy fatigue

Chapter 4

Methods

This chapter will be discussing the methods employed throughout the project where the underlying knowledge and literature has been spoken about in the previous chapters 2 & 3. Here, more detail shall be shed onto the equations and processes used to develop and run the models used for the results generated, this will be done over two parts, analytic modelling and numerical modelling.

4.1 Analytic modelling

This section of the thesis will be describing the actions taken in order to perform the analytic modelling for the research, this will be further build on the knowledge previously mentioned throughout the thesis. Here will be an in-depth presentation of how the modelling was performed and why it has been done in such a manner. This is a key area to the research as here some of the CLT experiments and calculations were performed on the composite materials and beam theory in terms of a blade.

4.1.1 Laminated composites

This part of the methods is ensuring the material of the wind turbine blade can be modelled correctly and with high accuracy. Starting with that of the classical lamination theory produced in a code format via freeware namely SciLab[1]. The equations mentioned in 3 are deployed here along with those featured in the introductory section to this chapter. Furthermore to the knowledge gained within section §2.2, here it will be expanded in terms of understanding to the materials used within the thesis. One of the equations to come

[1]available: https://www.scilab.org/

to light during the experimental stages is named the rule of mixtures. In equation (4.1) it calculates the overall elastic moduli of the composite material based on the elastic moduli of the fibre and the matrix along with their volume fractions:

$$E_C = E_F V_f + E_M(1 - V_F) \tag{4.1}$$

where E_C is the elastic modulus of the composite as a whole, E_F is the elastic modulus of the fibre with E_M is that of the matrix, and V_F is the volume fraction of the fibre [75]. The use for this within this thesis will help determine the overall material properties of the composite, this can be used as a validation for the overall material properties as well as being able to set up the material correctly. Equation (4.1) has been defined when in the parallel mode or when in the longitudinal direction, when looking in the transverse namely series mode then the equation will be presented as equation (4.2):

$$\frac{1}{E_C} = \frac{1}{E_F} V_f + \frac{1}{E_M}(1 - V_F) \tag{4.2}$$

where in equation (4.1) and (4.2) the nomenclature is the same. As mentioned in chapter 2, composite materials section, equation (2.12) requires another matrix in order to convert between the engineering strains and the tensor strains. When introducing the Reuters matrix, this avoids having to correct the values calculated manually, thus by employing the matrix it allows for transformation between the two types of strain [41]:

$$\Big[R\Big] = \begin{bmatrix} 1 & 0 & 0 \\ 0 & 1 & 0 \\ 0 & 0 & 2 \end{bmatrix} \tag{4.3}$$

or

$$\Big[R\Big]^{-1} = \begin{bmatrix} 1 & 0 & 0 \\ 0 & 1 & 0 \\ 0 & 0 & \frac{1}{2} \end{bmatrix} \tag{4.4}$$

this is also a method of correcting the strains that has been used by National Aeronautic and Space Administration (NASA) [66], named Reuters matrix from David Roylance [41]. This will prove to be a useful equation in order to confidently transform between the engineering and tensor strains. This matrix will become important when calculating the stresses and strains in both the global and local coordinates when it is multiplied with the T matrix.

Global stresses and strains are denoted with the subscript x, y, and xy while the local variables are exclaimed by 1, 2, and 12. Global coordinates are those of the complete structure or of a subcomponent of a structure, these will be used to calculate the local variables with the use of the transformation matrix [76]. Using equation (3.31) we can find the strains within the laminate, furthermore this can be used to find the stresses using equation (2.14). Now that the global stress and strains can be calculated for the composite, finding the principal stresses and strains for the system can be performed. This is done by finding the eigenvalues for the matrix. The eigenvalues are determined by the following

$$\lambda x = Ax \tag{4.5}$$

where the number λ is an eigenvalue of A, thus finding weather the vector x is affected by the multiplication of A [77]. Upon finding the eigenvalues the $1st$ and $3rd$ principal stresses and strains can be calculated. Where the in the case of composite materials, $1st$ principal is in the direction of the fibres, example being at a 45° angle for the fibre the $1st$ principal will be referring to that angle and direction. The $2nd$ principal is out of the plane, an example being that this would be through the thickness of a composite. Alternative to the $1st$ is the $3rd$ principal which is in the opposite direction to the fibres, with the same example in a 45° angle layer the $3rd$ principal would be 90° out of phase at $-45°$. Taking knowledge a 0.1% displacement was placed upon the composite in the x directions utilizing equation (3.30) whereby N_x is the applied displacement. Thus, resulting in an experiment which can have the results compared to that of numerical modelling. Table 4.1 shows two different layup sequences, where the first is going to be used as a benchmarking sequence, the latter being the layup sequence used for the main set of simulations. Layup 1 contains a total of 4 plys to form a laminate, whilst layup 2 contains a total of 40 plys; the first half will run in the order described, then mirror the remaining half. A CLT script run via SciLab made use of two materials and two different layup sequences to ensure the modelling is being carried out correctly, Table 4.1 shows those used within the modelling process. While Table 4.2 shows the materials used not only in analytical modelling but through out the work presented; ν_{yz} of glass fibre has been assumed to be the Epoxy resin where through the layers this will be the primary Poissons ratio within the full layup sequence [78].

Name	Sequence (°)
Layup 1	$[45, -45, -45, 45]$
Layup 2	$[90, 45, 0, -45]$

Source: [40]

Table 4.1: Material layup sequences

Material Property	Aluminium	Glass fibre	Unit of measure
E_x	70.0	24.4	GPa
E_y	-	6.87	GPa
E_z	-	6.87	GPa
ν_{xy}	0.30	0.32	-
ν_{xz}	-	0.32	-
ν_{yz}	-	0.32	-
G_{xy}	-	2.89	GPa
G_{xz}	-	2.64	GPa
G_{yz}	-	2.64	GPa

Source: [40]

Table 4.2: Material properties

4.1.2 Cantilever beam model

Developing the models discussed within chapter 3 for bending theory, it is mentioned that the blade can be modelled as a cantilever beam. The reasoning for this is a cantilever beam connects to the wall the same way a blade would connect to the central hub for the system. Taking this knowledge the analytical model with model the blade as a beam in terms of bending. Using SciLab as done in previous analytical models, equation (3.6) was modelled in-order to produce a bending moment on the blade. This method takes into account of the basic dimensions of the blade along with some of the material properties. The beginning of this utilizes the airfoil profiles to develop a beam, finding the second moment of area and then having a load applied. The main to airfoil profiles chosen are NACA2414 & NACA2415, seen in Figures 4.1a and 4.1b where these are similar designs for turbine use, the length of this blade will be 4200 mm. The chosen applied load here is 1000 Newtons, as a baseline test to develop a model based on the stiffer of the two profiles. Further to this, these are also

recreated within ANSYS for comparison data.

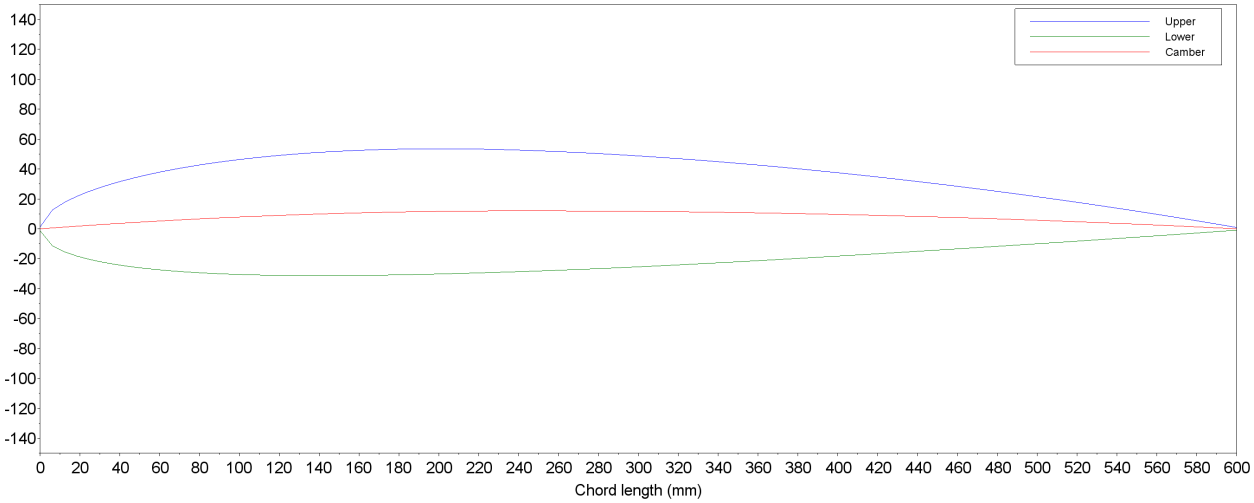

(a) NACA 2414

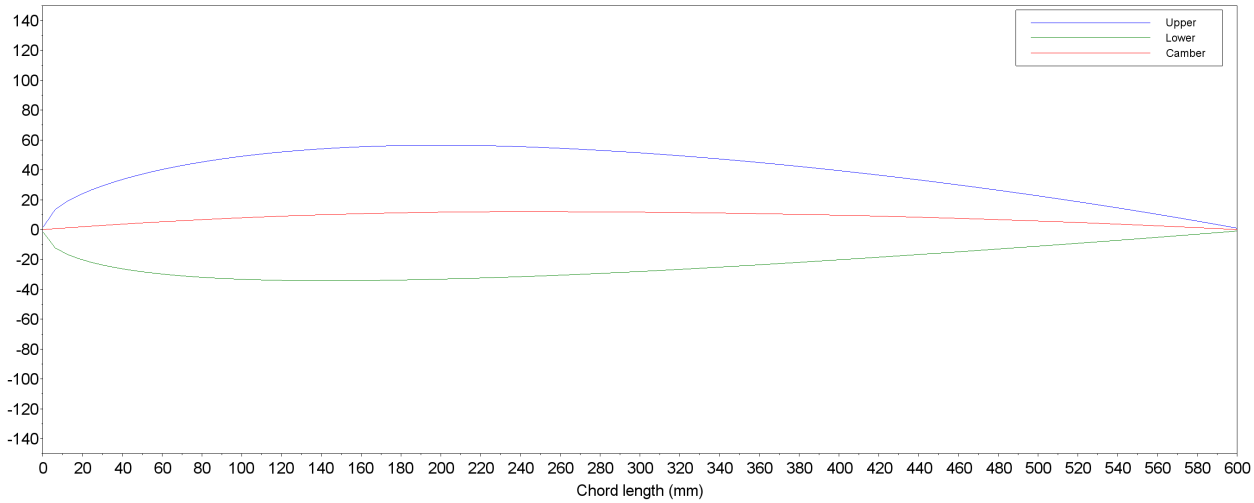

(b) NACA 2415

Figure 4.1: NACA aerofoil profiles

4.1.3 Castigliano's

One of the methods being employed within this thesis is the application of Castigliano's theory as mentioned in §3. Although to ensure this theory can be applied into the tapered section of the blade a few alterations have had to take place to ensure compliance. As previously discussed equation (3.25) describes how the displacement can be calculated with this theory, in order to allow the method to work the bending moment used must be calculated for each variation of chord length along the span of the blade. The way in which this has been

implemented into the system uses the following:

$$b(z) = b_t + (b_r - b_t)\frac{z}{L} \tag{4.6}$$

where $b(z)$ is the breadth of the chord at any point along the blade at distance z, b_t / b_r and both the breadth of the chord length at the root (r) and the tip (t) of the blade, while L is the total length of the blade used. During the application of Castigliano's it is important in this instance to assume that the fictitious moment, M_p, at the end of the blade is equal to $-z$. Allowing this applies the moment as 1 to negate the interference of itself.

4.2 Numerical Modelling

The following section to this thesis will be discussing and exploring the methods used for generating numerical models of the required WTB. Here, will cover material and blade modelling using a couple of different packages, although all from the ANSYS brand. The key aspects for this section is the materials to be modelled in a way that it is accurately representative of that in field while the blade profile is that of the more structurally sound in relation to bending theories previously approached.

4.2.1 Laminated composites

During the modelling of the ANSYS APDL a code is created which will be used to run the full model, the first steps of this are named pre-processing where this is setting up material properties and geometry. The starting point for all of the code is selecting the correct element type, for this the type chosen is named Shell281. This element type has been selected for being applicable for thin to moderately thick shell structures, this type of element is appropriate for the laminated composites. This element type has eight nodes each with six Degrees of Freedom (DoF) which can be rotation and translations in the x,y and z axes [79]. The element is defined as a shell with the eight nodes named I, J, K, L, M, N, O, and P with the following geometry where T is temperature at each corner, unless specified this defaults to be equal all around [79].

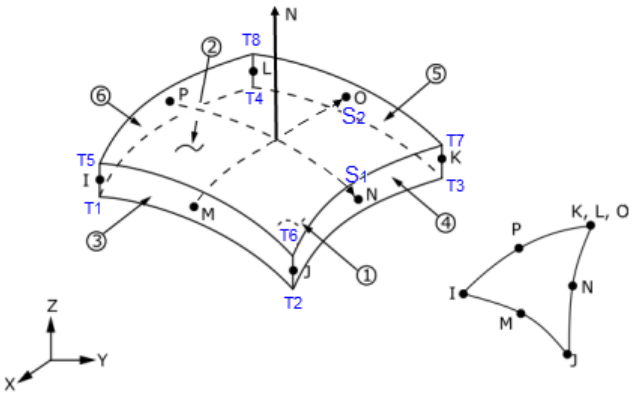

Source: [79]

Figure 4.2: SHELL281 geometry

Where as the shell elements selected in ANSYS Workbench is SHELL181, which is a four node element with six DoF within each of the nodes; same as SHELL281. The element is defined as the shell through the four nodes, named I, J, K, and L. Other than the number of nodes within the SHELL181 type differing from SHELL281, the remainder of the element type stays the same; Figure 4.3, displays the shell element.

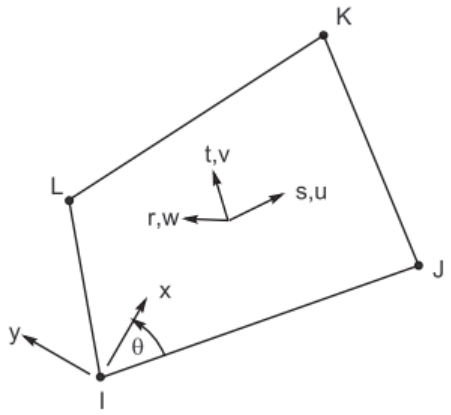

Source: [79]

Figure 4.3: SHELL181 geometry

The main difference between SHELL281 SHELL181 is that the latter does not contain mid-side nodes in the centre of the shell, the uses of this within composite material testing would show deformation within that area. Both of these element types are h-type elements

although SHELL281 is a more refined when in comparison to SHELL181. Thus, the refinement of these elements through the use of the mid-side nodes effects the accuracy of the element and ultimately the results therein [70]. The other preprocessing to be carried out involves the generation of the material and the lay-up sequence in which to be used, see Table 4.1. The manner in which the material is set up is by manually inputting the material properties. There will be two materials supplied to the APDL code as shown in Table 4.2. The materials to be used are going to be applied to a test token to ensure the correct properties are introduced. The dimensions of the full size token are as seen in Table 4.3 along with the quarter size which will be used in conjunction with symmetry allowing for a less computationally expensive experiment.

	Full size model (mm)	Quarter size model (mm)
Length	100	50
Height	150	75

Table 4.3: Material token dimensions

Once the correct material and geometry had been set up, the boundary conditions needed to be applied. In order to do this, some of the lines within the model will have to have the boundary conditions set to simulate that of being a continual plane in the correct direction. Figure 4.4a shows the model built by using the code, while Figure 4.4b shows where this would section would be within the full scale model. Furthermore, the other boundary conditions have been set up to produce a 0.1% strain to either compress or extend the test piece, in an identical test carried out in the SciLab code.

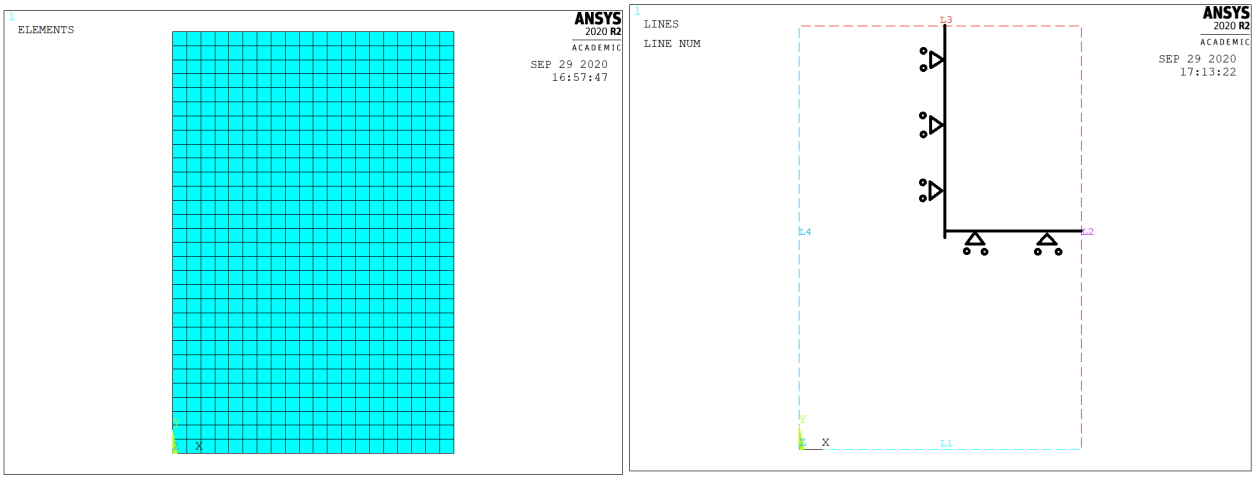

(a) Quarter model token

(b) Full model token

Figure 4.4: Quarter and full token models

Looking at Figure 4.4a the elements are visible, with a total node count 1901 and an element count of 1871. Seen in Figure 4.4b the quarter model of the token will employ symmetry via boundary conditions, the conditions used are as follows, where line 1 is the bottom line moving around in a clockwise direction finishing with line 4 being the furthest left line.

Boundary condition	Line 1	Line 4
Displacement in X	-	✓
Displacement in Y	✓	-
Displacement in Z	✓	✓
Rotation in Z	✓	✓

Table 4.4: Boundary conditions

When reviewing both Figure 4.4b and Table 4.4 it shows how the boundary conditions con-inside for the correct symmetry. Although, here this does not show any of the 0.1% strains placed within the system. As this could be done in either the x or y axis an *if* statement is used to select the correct line and strain involved in the system. The use of the *if* allows for a change in direction of the displacement. Allowing the overall system to be solved, the solution to this is to find the mechanical properties of the overall material as a whole. Thus using the sum of the reaction force for the opposing line, example being if the displacement is in the X direction, the line at the bottom of the token will be measured this value is used to help calculate the Young's modulus. In order to calculate the rest of the material properties,

the traverse and parallel strains are calculated for the Poisson's ratio as in equation (2.4). This code finishes with a pop up message with the calculated results to allow an easier view of the results. The post-processing carried out was in order to evaluate the results produced, these were compared against those of the CLT equations discussed previously. Where by comparing the results between classical lamination theory and APDL code will be used to compare the values and where the material and layup models are accurately developed. The main post-processing data that was of interest for ensuring the accurate development of the models are X & Y direction of stress with XY shear stress. Also, the $1st$ and $3rd$ principal stresses are the Eigenvalues of the stress tensor used. These are the two sequences to be tested as outlined above in order to develop a reliable and accurate material model with the understanding that these correlate with sound engineering theory such as classical lamination theory.

4.2.2 Benchmarking

In-order to ensure that the correct NACA profile has been selected, further experimentation using said blades will need to be conducted. Analytic models have already been produced and generated results, this is to be carried out in a numerical methods. The main tool used for this is ANSYS Workbench, whereby the full 4200mm blade is built using NACA2414 & NACA2415 as a surface. During the modelling of the blade it is split into three surfaces, the blade structure with a top and bottom while a separate one for the spar supporting structure running down the span of the blade. Each of these surfaces are 5mm in thickness. The reasoning for this approach is to allow the correct application of the boundary conditions while also being able to create paths on the structure to export data for comparisons with analytical data. Figures 4.5b and 4.5b shows the two blade models.

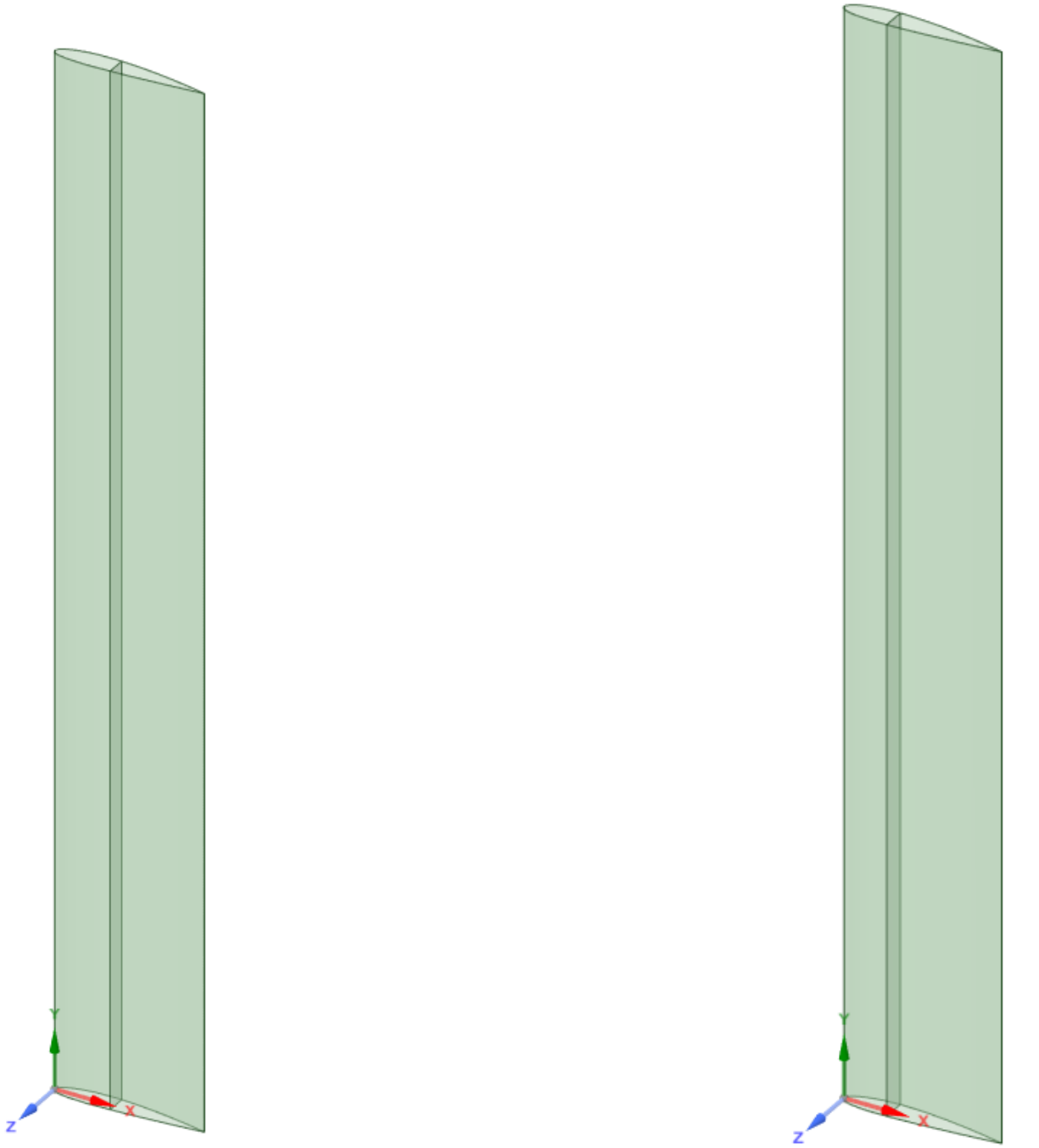

(a) NACA2414 Geometry

(b) NACA2415 Geometry

Figure 4.5: NACA2414 & NACA2415 Geometries

As seen in Figures 4.5a and 4.5b the supporting spar structure is placed at the highest points of the blade profile, the reason for this is to add the most support as possible. Fur-

thermore to this, the material applied to this is the standard aluminium alloy found within the ANSYS material library, Table 4.5 shows the properties of such[2]. The other materials applied to this are those found in Table 4.2 for glass fibre using layup sequence 1 found in Table 4.1, the thickness of each layer is 1.25mm allowing for a total thickness of 5mm, matching that of the aluminium. When using the composite, the supporting spar structure will be not be included as this is not accounted for during the SciLab code.

Material Property	Aluminium	Unit of measure
E_x	71.0	GPa
ν_{xy}	0.30	-
G	26.7	GPa
K	69.6	GPa

Table 4.5: ANSYS aluminium alloy material properties

Furthermore the boundary conditions for this experiment were applied to the system in order to develop the model. This had the same boundary conditions placed on it that the analytical model mentioned above, this is a cantilever beam fixed at one end while a force of 1000 Newtons that is applied to the top surface hence the splitting of the blade into multiple surfaces. As this is a model within a FEA software a mesh is needed, the over all nodes and elements within both models comes to 2284 & 2086 for NACA2414 respectively while NACA2415 is 2312 nodes and 2113 elements for the model. This was achieved by both devices having a regular mesh and a face mesh applied to the outer two surfaces to ensure the mesh is quadrilaterals over the whole model. Figure 4.6a shows the mesh applied on NACA2414 with Figure 4.6b showing the boundary conditions applied within the system.

[2]K is the Bulk modulus

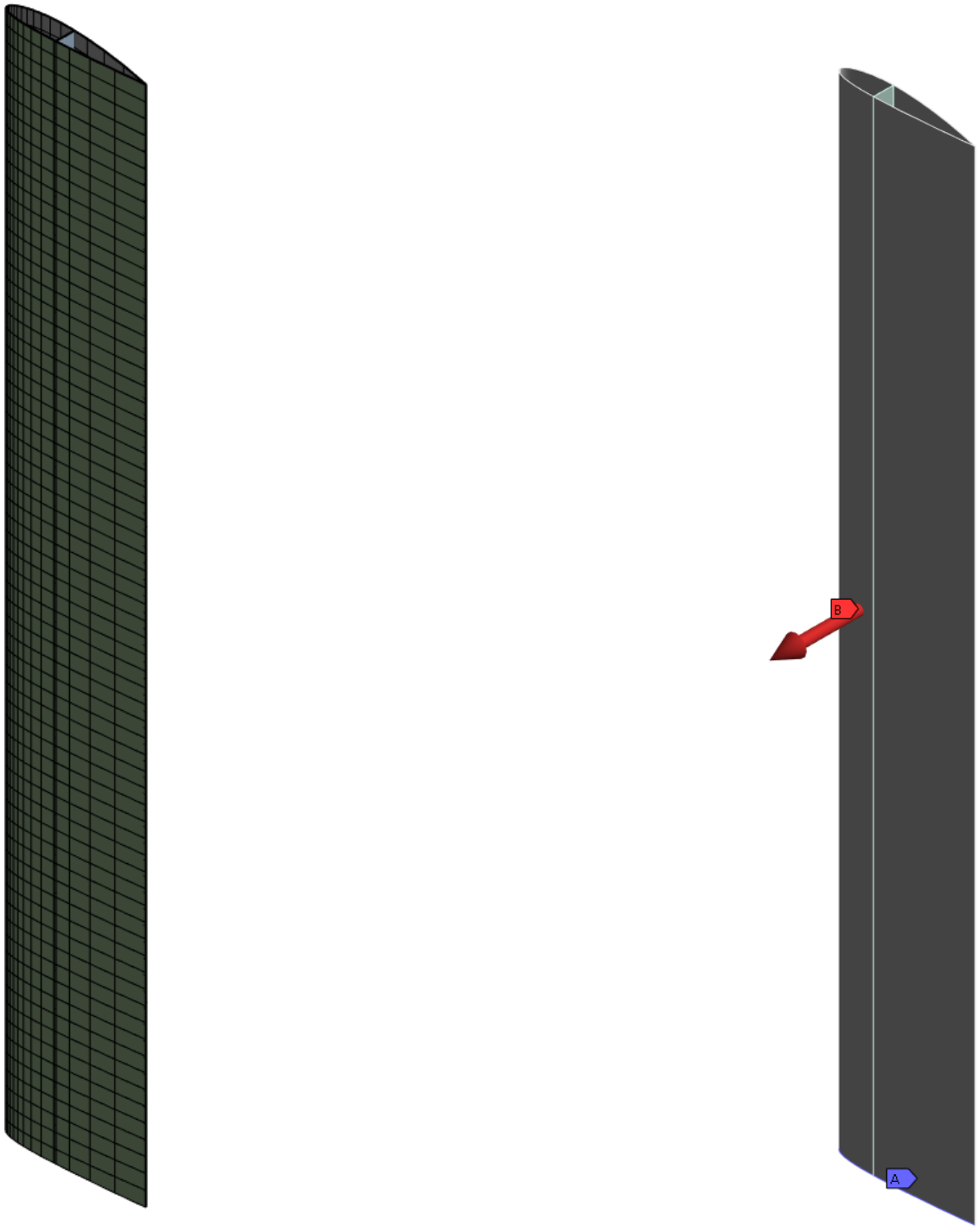

(a) NACA2414 Mesh

(b) NACA2415 boundary conditions

Figure 4.6: NACA2414 mesh & NACA2415 boundary conditions

As seen in Figure 4.6b here in, A is the force applied whilst B is the fixed support. The results expected to gain from this are the stiffer model of the two in-order to use that design to progress onto the tapered model. In the next steps of applying the composite to the blade it has a change in the manner of calculating the amount of bending performed by the blade. Usually during bending for a isotropic material the normal modulus of elasticity would be used, however when using composite materials, this is swapped out for a different value named the flexural modulus. This value replaces the regular Young's modulus value as seen in equation (3.1) with that of equations (4.7) & (4.8):

$$E_{fx} = \frac{12}{t^3 D'_{11}}, \tag{4.7}$$

$$E_{fy} = \frac{12}{t^3 D'_{22}}, \tag{4.8}$$

where E_{fx} & E_{fy} are the flexural moduli in the corresponding x and y axes, t is the thickness of the whole laminate and D is the inverse of the matrix [40] found in equation (3.29). The method of using the correct one for each case depends on the orientation of the blade, if the blade runs in the y direction then the E_{fy} value would be used. The lay-up sequence applied to this blade is that of lay-up sequence 2, c.f. Table 4.1, although the geometry used with this removed the supporting spar structure allowing for a multitude of methods to be explored in order to verify and validate the results captured. Using the same method as above the blade has the force applied and the martial used is the full layer composite as well as applying it as an orthotropic material using equations (4.7) and (4.8); using these equations the full layup sequence thickness will be applied to a surface within ANSYS Mechanical, giving the desired thickness to each surface ensure that the numerical analysis would be calculating the moduli as a plate. Here it should be discussed that the advantages of using the two types of material for this work will allow for a direct comparison *in-silico* of modelling the composite as a full layup sequence alongside a representative orthotropic equivalent. As previously discussed, materials may be modelled as either the full layup ABD matrix inclusive, or alternatively, as a homogenous model with generalized elastic properties (i.e.: an orthotropic equivalent). Although, using the orthotropic equivalent material will only give results for the structure deformation and not the ply-by-ply stresses that may be present within the full layup sequence; the importance of using the orthotropic equivalent may be evident during the simulation of fatigue in these devices. Ply-by-ply stress exists within the full composite layup when under bending; tensile and compressive bending will exhibit ply-by-ply stress due to the laminate experiencing delamination via shear or buckling. Varying levels

of stress will be present within the material dependent upon the orientation of laminate layers. The method of applying the full layup sequence will be modelled through the utilization of ANSYS Mechanicalâs layer approach, allowing for individual composite layers to be added at required angles (as per Table 4.1); whereas the orthotropic equivalent has been applied as new material, with a prescribed thickness supplied to the surface model, representing that of the full composite layup sequence.

Another approach taken is to apply the same theory to a box section of the same length with an identical I value found in equation (3.6), Figure 4.7a shows the box section geometry used within this test with the mesh applied. Using the parallel axis theory the dimensions for the new box section would be calculated as 600mm matching that of the chord length of the blade while the height of the section is calculated to be 66mm in order to provide the same I value as the blade. These experiments will define if the materials and straight blades are modelled correctly and that the methods are able to move forward within the research.

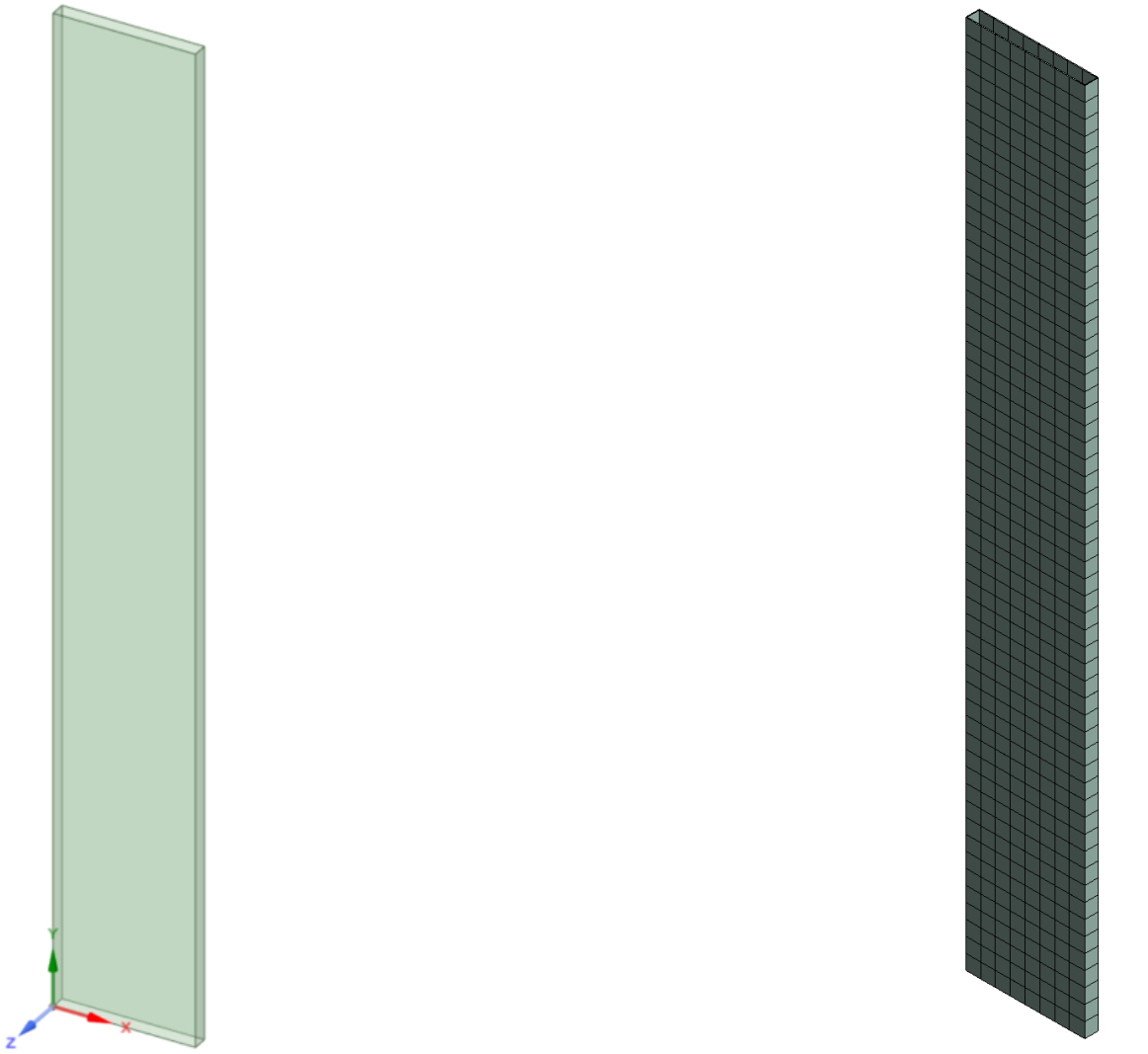

(a) Box section geometry

(b) Box section mesh

Figure 4.7: Equivalent box section geometry and mesh

4.2.3 Tapered section

The stiffer design out of the two tested above is taken forward to be used as a tapered blade with the same span at 4200mm. Although the difference here with the taper is that over the span the chord length of the blade half's at the tip. Figure 4.8 shows the new geometry used for these experiments, as seen this shows how the chord of the blade at each end differs.

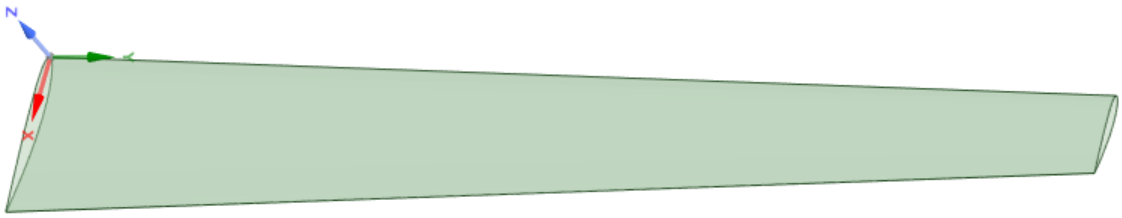

Figure 4.8: Tapered blade geometry

Although, as seen in Figure 4.8 the blades orientation is rotated around the x axis when compared to those of Figures 4.5a and 4.5b as when applying a layered composite within ANSYS Mechanical the software defaults to applying the laminate through the z axis. Moving the geometry into the Mechanical component of ANSYS Workbench, the following is the procedure the model has gone through to ensure it is ready for the computational simulation. First stage is setting composite material, this is using the second layup sequence found in Table 4.1 with the symmetry. The layup sequence is applied to two surfaces, these being the wing top and bottom skins, where Table 4.2 states the material properties of the glass fibre used. Table 4.6 shows the details for each of the surfaces involved for the model.

Model component	Material	Thickness (mm)
Upper wing	Glass fibre	5
Lower wing	Glass fibre	5

Table 4.6: Tapered blade material

As the model used is in separate surfaces these need to be joined together within ANSYS to allow them to capture the whole geometry interacting with one another. This is carried out by selecting the correct edges to mate together and applying the correct conditions. Here, one will need to be made, the leading edges of the blade along with the trailing edges these being bonded together. This is a key step within the modelling as without it when the wind force is applied, the moving structure will not interact but more collide with the remaining sections. Figure 4.9 shows highlighted lines when connections between surfaces have been invoked, this depicts the connections between the leading and trailing edges for both the upper and lower surfaces.

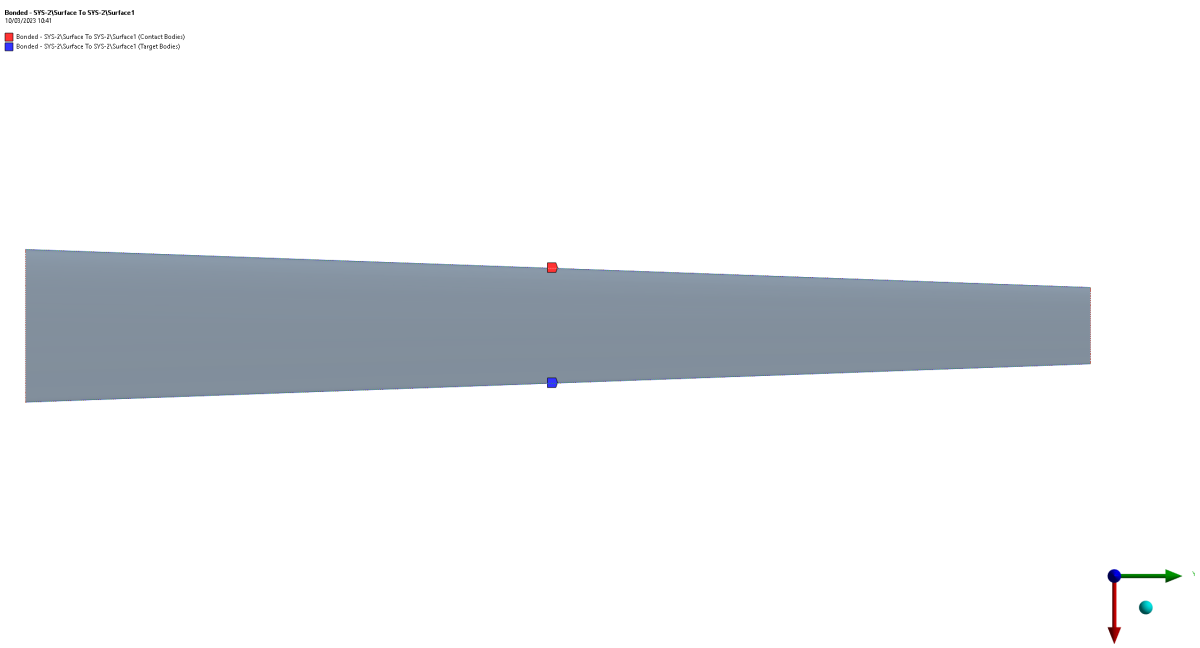

Figure 4.9: Connecting points

The meshing of the blade is the following process, now that the structure as a whole is interacting correctly. This took a similar path to that of the straight blade however with the tapering of the blade extra steps are required in-order to allow a mesh independent study. As previously, a face mesh is applied to the blades surfaces. Furthermore, the leading and trailing edges of both the upper and lower surfaces have a bias applied, this not only keeps the elements running along the chord of the blade. This method also allows for a higher density of elements to be placed near the root of the blade, where the higher stresses would be expected. Figure 4.10a illustrates how the mesh looks on the blade. Another aspect of the mesh that is less visible from Figure 4.10b is the edge sizing applied to the root of the blade in order to retain the curvature of the blade profile. This has been achieved by increasing the number of elements about the area, by increasing these there are more, shorter elements to generate the curve. Compared to if a lower count was used this would cause steep angles on the profile, thus losing shape. Figure 4.10b shows the number of elements about the profile. The total count of nodes and elements came to 9256 and 8903 respectively. The mesh has a face mesh & bias applied to it, the purpose of doing this is to focus the refinement of the mesh at the root of the blade, where it is assumed that the most stress will occur in the device; the element size used for this and further studies has been set to 100 millimetres. The mesh used within these studies has been subjected to a mesh sensitivity study which should allow the convergence of these results to be unaffected by a further refined mesh; this also ensures that

the mesh is optimal for computational expense without the overuse of nodes and elements.

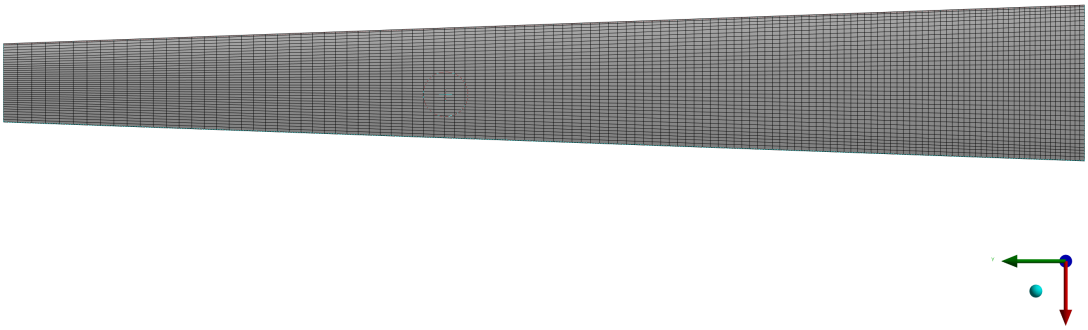

(a) Mesh

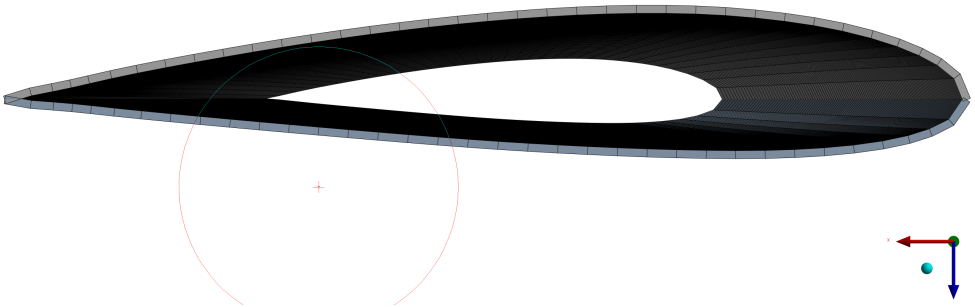

(b) Profile curvature

Figure 4.10: Tapered blade mesh

Further to the setting up process of the model is crafting the boundary conditions for the simulations. The first boundary condition applied is the fixed support at the root of the blade, in the same manner as the straight blade. The second boundary condition imposed is the wind force calculated using equation (4.9) where the area of the wing has been applied using equation (4.10):

$$F_w = \frac{1}{2}\rho v^2 A, \tag{4.9}$$

$$A = (\text{Span})(\text{avg. Chord}) = (\text{Span})\frac{(\text{Root chord} + \text{Tip chord})}{2}, \tag{4.10}$$

where ρ is the density of air, v^2 is the velocity of the wind and A is the area, as per equation (4.10). Using equation (4.9) it is found that the force to be applied is 81.9 Newtons, this is calculated using a class II wind turbine average wind speed of 8.5 meters per second [80]. However, for the purposes of the experiments, this value has been increased to a total of 100 Newtons. This second boundary condition is to be applied on the upper section of the blade similar to that of the straight blade previously. Figure 4.11 shows how these are acting upon the blade within ANSYS, where the red arrow A is the wind force as per equation (4.9) while the blue lines are the fixed support. Overall this builds the tapered blade model for testing within ANSYS.

Figure 4.11: Tapered blade boundary conditions

4.2.4 Wind turbine blade modelling

Here, the tapered model will be repeated with a modified geometry, this is to represent a more accurate wind turbine blade as seen in Figure 1.7. Although the modelling here does not take into account the connecting mechanism to the hub of the device, Figure 4.12 shows the blade design using the airfoil profiles within ANSY SpaceClaim. The blade geometry is the same as that in Figure 4.8, including two airfoil profiles however, the profile at the tip of the blade has a 5 rotation applied whereby placing the leading edge of the blade is lower than that of the trailing edge.

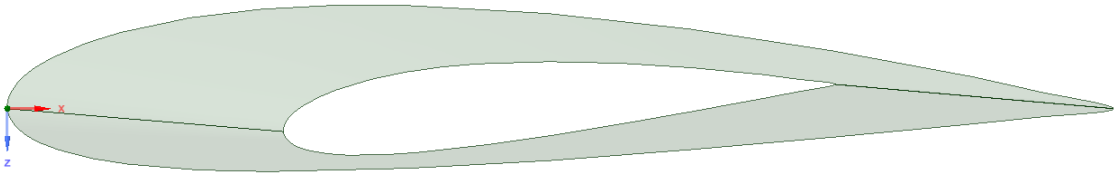

Figure 4.12: Twisted blade profile

The same 100 Newton force presented applied in a UDL fashion to the top half of the blade. The deflection and stresses experienced by the device will be analysed to ensure the successful modelling of the blade.

4.2.5 Fatigue

Further the fatigue properties are to be calculated utilizing equation (3.59) mentioned in chapter 3 also. Here, the blade will be subjected to fatigue loading through ANSYS Workbench Mechanical and the life and damage of the blade will be assessed. The method of calculating the required values has been done as follows in equations (4.11) on wards:

$$f = \frac{2\pi V n}{L} \tag{4.11}$$

where f is frequency with n in the total number of blades in the system at a wind speed of V, while L is the length of these blades. The value obtained with this will be used to determine the total number of cycles to failure, N_f, throughout a number of changes of the blades; assuming these devices do not stop during this. Here, this would allow an average wind speed to be 8.5 meters per second, while the blades will remain at 4200 millimetres long [80]. The assumptions made within this work will be based on these devices only being subjected to normal operating conditions during the full life of the wind turbine system; assumed to be 25 years. Hence, no other fatigue factors such as extreme weather, manufacturing errors, and temperature are to be considered. Furthermore, it is assumed that the failure criteria of these WTBs will be the matrix material, due to the reduced material properties in comparison to glass which may result in delamination through ply-by-ply stress. Where at 1% of the matrix's original ultimate tensile strength value will be the fatigue limit of the material; the first 100 cycles will simulate no fatigue occurring. These assumptions will be applied to a strategy of replacement blades that may be implemented during the wind turbine systems'

life, *i.e.*: the blades may be replaced 5 times through the systems life, or alternatively a single replacement. Table 4.7 shows the design life for each device depending upon the replacement strategy employed.

Replacement Strategy	Design Life (years)
1	12.50
2	8.33
3	6.25
4	5.00
5	4.16

Table 4.7: Design life per replacement

Changing the design life of these devices will also affect the number of cycles to failure (N_f) for each replacement strategy, further affecting the Factor of Safety (FoS) expected from each of the design lives. The experiments will be carried out in the same operational window as the bending experiment as above using the fatigue tool within the FEA software. During this stage the mechanical factor of safety will be 2, ensuring that the same force is applied to the system, maintaining continuity.

Chapter 5

Results

Using the previously mentioned methods, the following results have been generated, here the results will be presented in detail although, any discussions will be reserved for a further chapter in this thesis. Here, equations with answers along with diagrams including graphs will be posted in combination with justifications of the results.

5.1 Material modelling

This section will be showing the results generated for the material modelling ensuring that the data used is accurate, correct and aligning with sound engineering theorems. Firstly starting with the underlying theory of CLT and then followed up with the Ansys APDL and Workbench simulations.

Using the equations of those found in chapters 2 and 4 for the classical lamination theory these were tested using an example found in literature [40] to ensure that the code is acting as it should. Further to this, it was then used to calculate a 0.1% strain within the system in the X direction using layup sequence 2 found in Table 4.1. The results produced can be found in Table 5.1, these will be looking at the overall material properties for the whole layup sequence, X & Y directions of stress, XY shear stress and first and second principal stresses. The above was recalculated using APDL and ANSYS Workbench where the results are also stored within Table 5.1.

Method		Value	Units
APDL	E	12786.2	MPa
(SHELL281)	ν	0.303	-
	σ_x	24.4	MPa
	σ_y	0.115	MPa
	τ_{xy}	0	MPa
	First Principal	24.4	MPa
	Second Principal	0.115	MPa
APDL	E	12786.2	MPa
(SHELL181)	ν	0.303	-
	σ_x	24.4	MPa
	σ_y	0.115	MPa
	τ_{xy}	0	MPa
	First Principal	24.4	MPa
	Second Principal	0.115	MPa
Workbench	E	12786.2	MPa
(SHELL181)	ν	0.3	-
	σ_x	24.4	MPa
	σ_y	0.115	MPa
	τ_{xy}	0	MPa
	First Principal	24.4	MPa
	Second Principal	0.115	MPa
CLT	E	12786.2	MPa
	ν	0.303	-
	σ_x	24.4	MPa
	σ_y	0.115	MPa
	τ_{xy}	0	MPa
	First Principal	24.4	MPa
	Second Principal	0.115	MPa

Table 5.1: Material results

5.2 Beam models

Here, this section will be displaying the results for all of the wing tests done both within ANSYS and SciLab in terms of both The straight blades for the purpose of bench marking as well as those generated from the tapered model, with the correct fatigue data applied.

5.2.1 Straight blades

During this part of the thesis, it will show the results of the straight blades from both analytic and numerical methods. This is used to determine the blade profile with the least amount of bending under identical conditions outlined in the previous chapter. The generation of results involved applying the above mentioned load of 1000 Newtons onto the top of the wing and taking the bending profile generated within ANSYS Mechanical to be used along with that of the analytical model developed within SciLab. Gaining validity to the results by having different methods of developing the same results. Firstly, NACA2414 is tested followed up with NACA2415 having the same conditions applied. Table 5.2 shows the results from both the ANSYS Mechanical simulations and the analytical data calculated from the bending theory.

Profile	Method	Value	Unit of measure
NACA2414	ANSYS	21.355	mm
	SciLab	22.262	mm
	Percentage difference	4.24	%
NACA2415	ANSYS	18.660	mm
	SciLab	19.439	mm
	Percentage difference	4.17	%

Table 5.2: Aluminium NACA2414 & NACA2415 bending

In order to show the bending over the length of the blade Figures 5.1 & 5.2 have been drafted. Using these Figures, it is clear that out of the two profiles suggested, NACA2415 is the stiffer and the more applicable for use of a wind turbine blade.

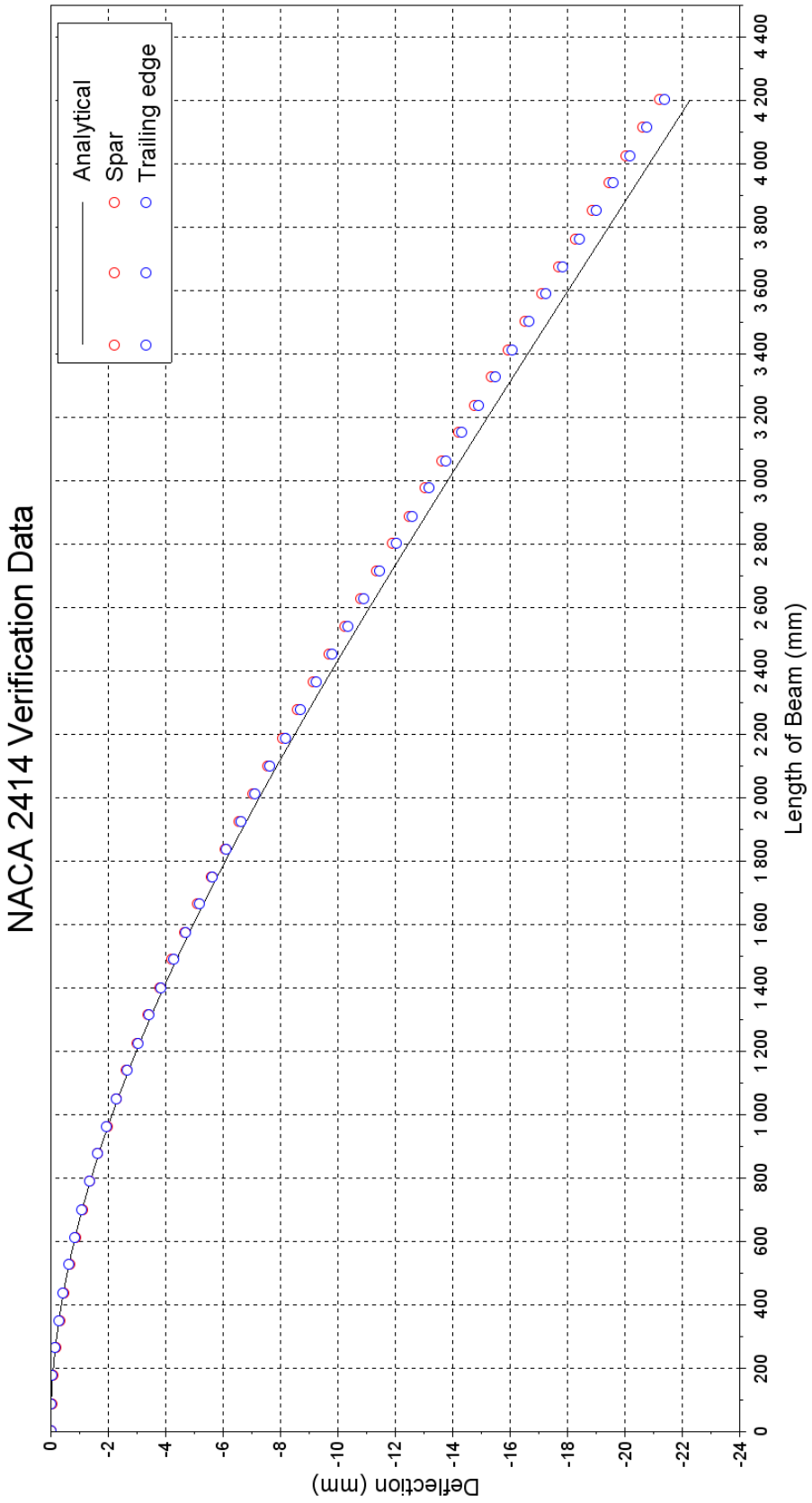

Figure 5.1: Aluminium NACA 2414 bending

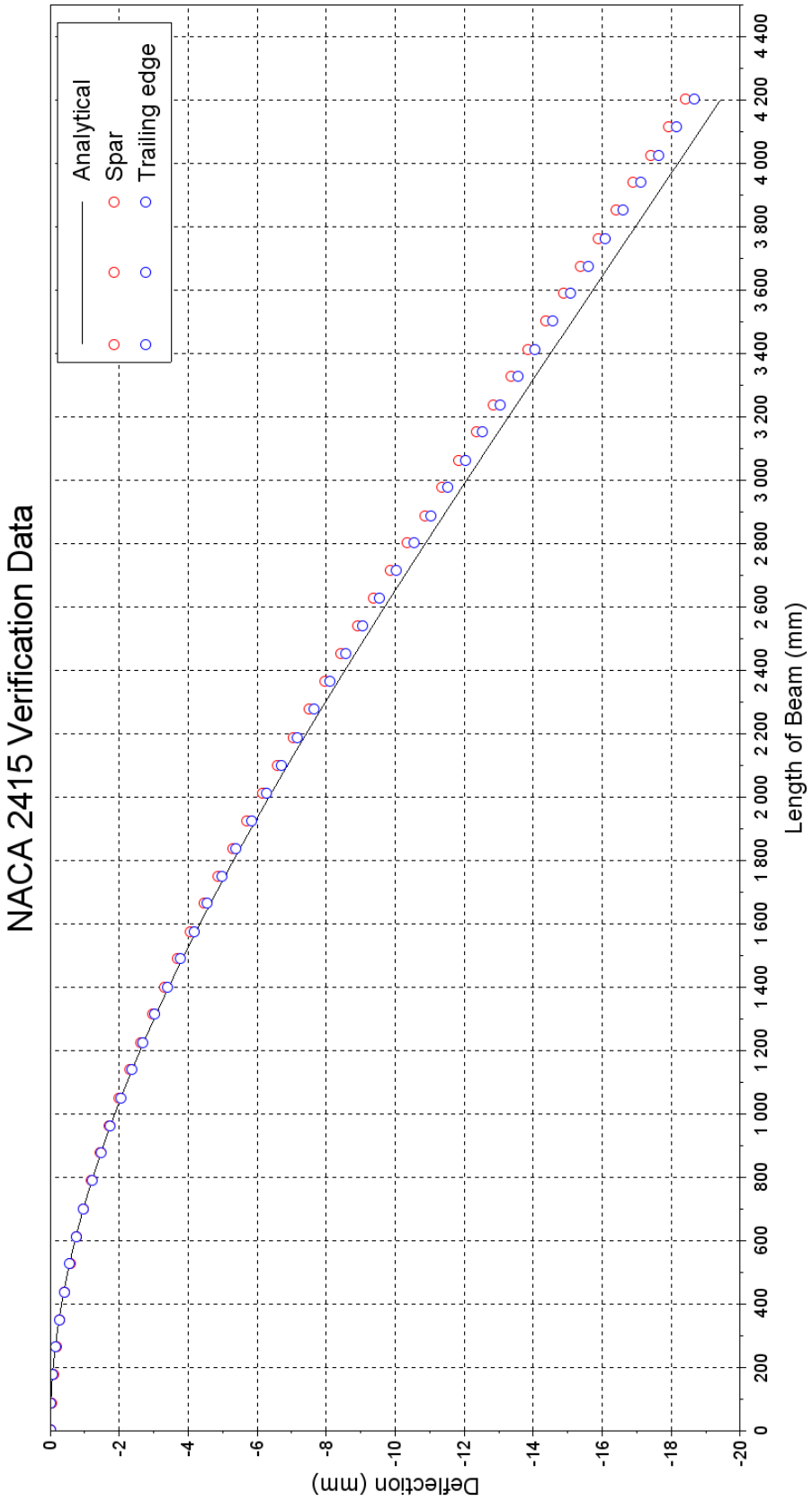

Figure 5.2: Aluminium NACA 2415 bending

The results when applying the composite material will contain more detail, as these will express the composite layup sequence as well as if the material was Orthotropic to compare these results against each other with the knowledge that the material has been modelled correctly. Table 5.3 shows the bending maximum bending of each material type along with bending theory calculations taking into account that found in equations (4.7) & (4.8).

Profile	Method	Value	Unit of measure
NACA2415	Orthotropic	114.51	mm
	Layup sequence	111.19	mm
	Bending theory	109.97	mm
	Eqv box	109.56	mm
	Runge-Kutta	111.31	mm

Table 5.3: Composite NACA2415 bending

Using Table 5.3, it is found the largest percentage difference between values is 4.32%. This shows that the results from ANSYS and theory have a correlation with one another. Figure 5.3 shows all of the data included within Table 5.3 as bending profiles over the length of the blade. Concluding the gathering of the results shown, the testing of the tapered blade can commence as the results of the straight blades are validated from theory, practice and modelling via ANSYS Workbench.

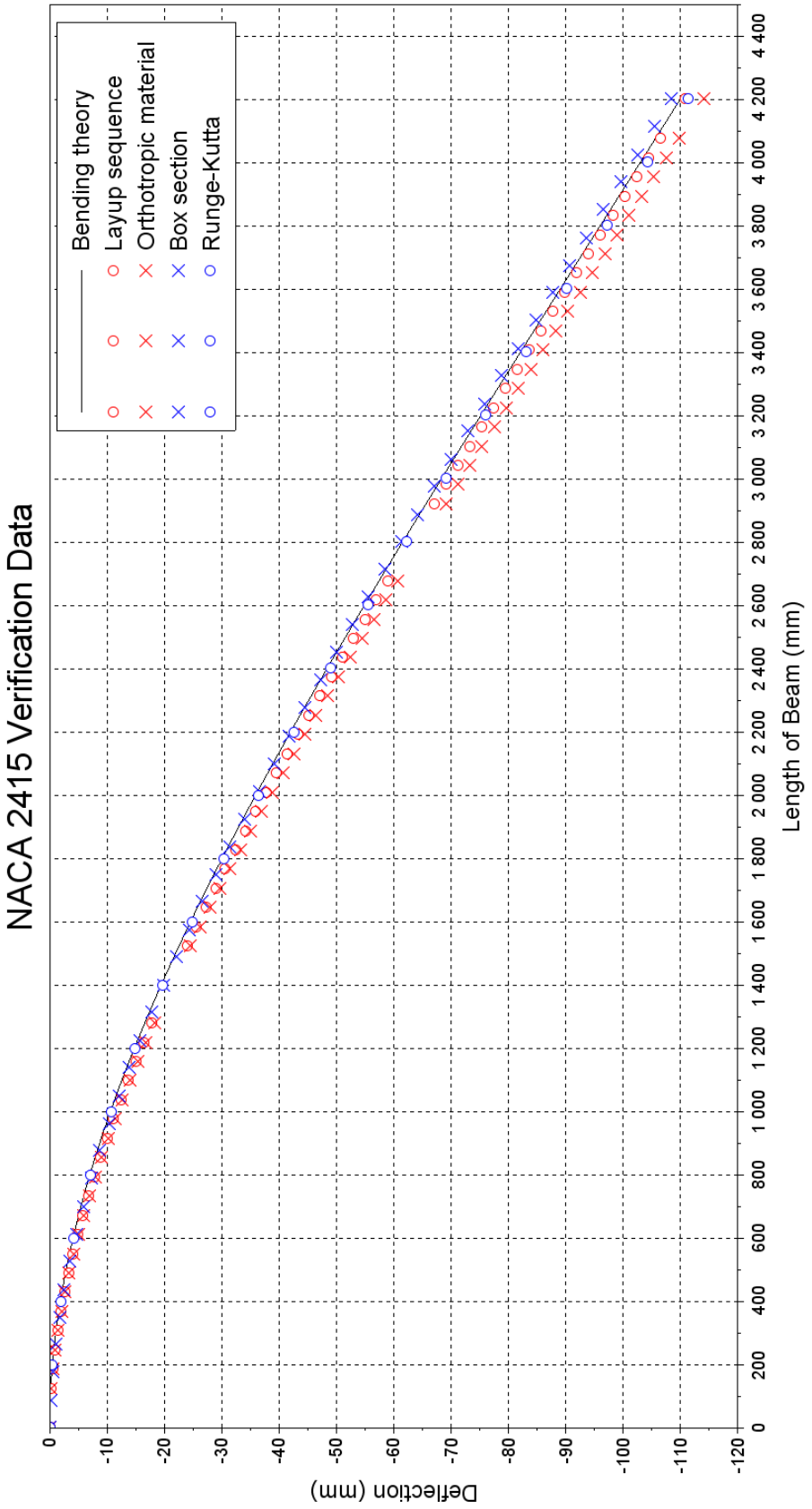

Figure 5.3: NACA 2415 Bending

5.2.2 Tapered blade

Following the straight blade testing, the tapered blade is the following results. As mentioned above, the tests conducted applied a wind force of 100 Newtons onto the top surface of the blade in order to invoke bending, this is then run through a number of different simulation methods including ANSYS Mechanical and Runge-Kutta via SciLab as well as an equivalent box section of the blade. Having already tested the two main blade profiles, here the profile that exhibited more structurally sound bending is being tested. Table 5.4 displays the results gathered from the various methods applied to this experiment.

Profile	Method	Value	Unit of measure
NACA2415	Orthotropic	12.16	mm
	Layup sequence	13.01	mm
	Runge-Kutta	12.52	mm
	Eqv. box Orthotropic	12.15	mm
	Eqv. box Layup sequence	12.99	mm
	Castigliano	12.63	mm

Table 5.4: Composite tapered blade

The above stated data shows that the largest percentage difference between the results as a whole is 6.6%, this is using an average height of 49.5mm for the section. Figure 5.4 demonstrates the bending profiles of all the methods through the whole span of the blade. Now this part of the work has been completed, the next stage is to move on to the bending of the full blade design, where this includes the taper and an angle offset from the tip as well as the fatigue modelling of the tapered blade.

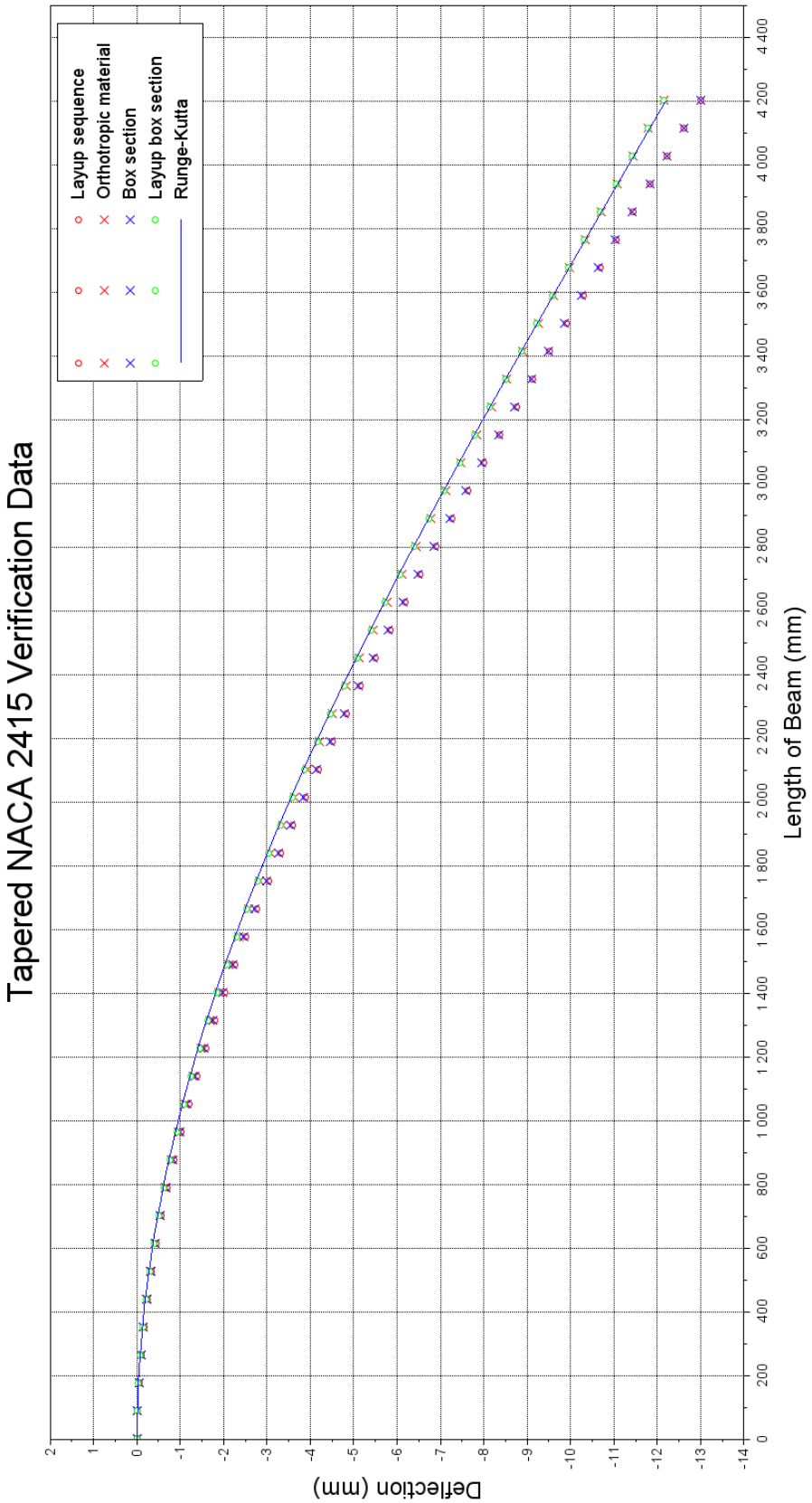

Figure 5.4: NACA 2415 Bending with taper

5.2.3 Tapered fatigue modelling

Using the aforementioned blade replacement profile, the fatigue data from the two methods employed is displayed in Figure 5.5, Table 5.5 shows the number of cycles to failure for each replacement when the 1% strength remains. In-order to achieve this, a force of 1400 Newtons is applied to met the assumption of mechanical factor of safety.

Number of replacements	cycles
1	15037906435
2	10025270957
3	7518953217
4	6015162574
5	5012635479

Table 5.5: Number of cycles to failure

The difference within these data are 10025270957 cycles comparing 1 replacement to 5 replacements. The minimum life from each of the devices is shown in Table 5.6, the results of these are in the expected place on the device thus, being towards the root.

Number of replacements	Power	Log Linear
1	3015.6	4.67×10^6
2	2802.3	3.70×10^6
3	2660.2	3.14×10^6
4	2555.0	2.76×10^6
5	2472.1	2.49×10^6

Table 5.6: Minimum blade life

Another aspect of the fatigue looked at the safety factor of the the devices, Table 5.7 details the minimum values for each of the employed methods. The simulations for each of the replacements found that the ANSYS stress factor of safety is 2 for all cases, this result has not been presented. The results shown from ANSYS Workbench are that of the 1, 3, and 5 replacements as these will be demonstrate the extremes and middle of these fatigue results.

Number of replacements	Power	Log Linear
1	0.04	0.35
2	0.04	0.30
3	0.038	0.27
4	0.036	0.25
5	0.034	0.22

Table 5.7: Minimum blade factor of safety

Figures 5.6, 5.7, and 5.8 detail the factor of safety for each of the models; 1, 3, and 5 replacements are employed. It can be observed that the minimum factor of safety is located within the base of the device, same to that of the minimum life.

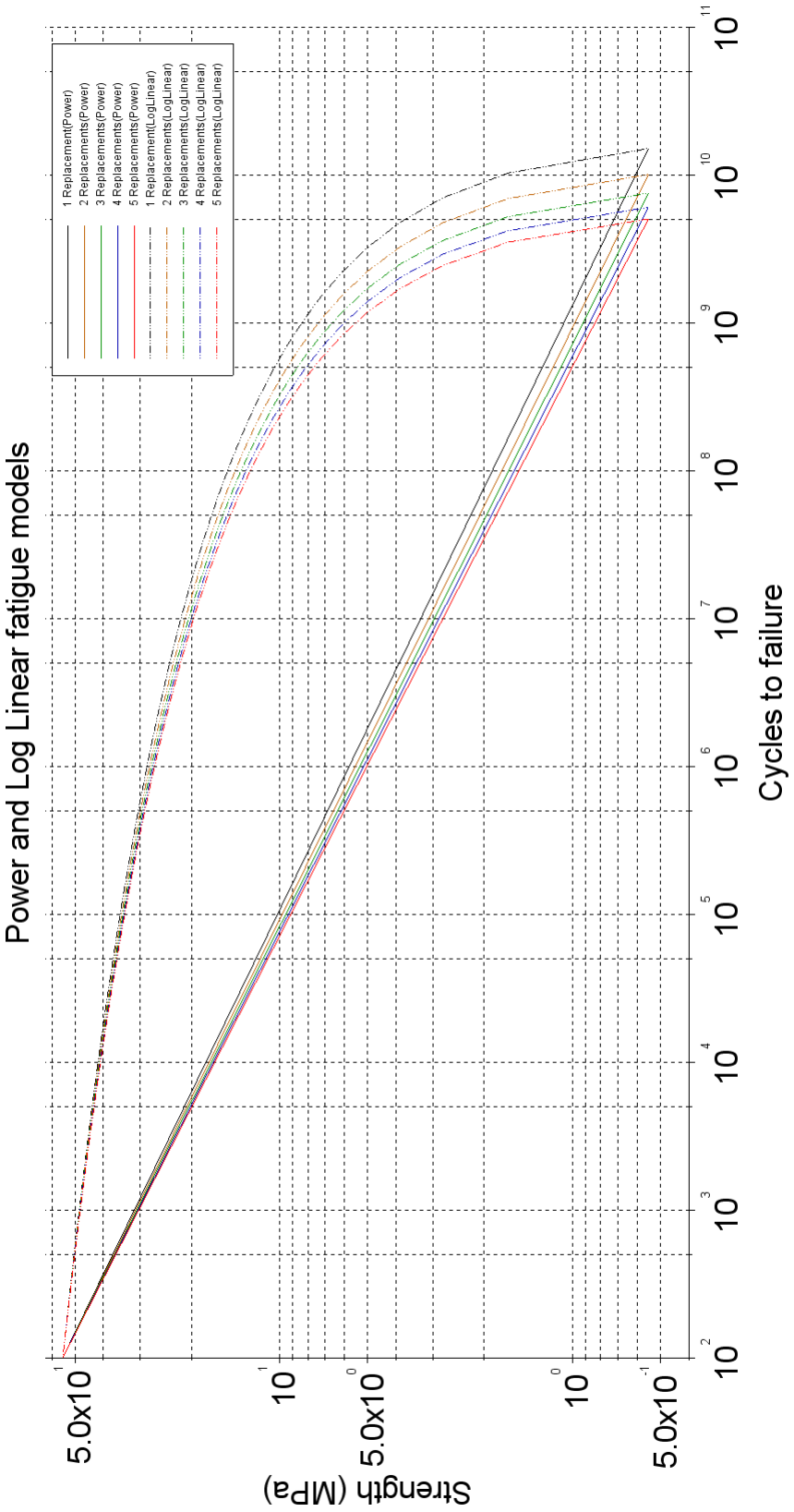

Figure 5.5: Power and log linear fatigue models

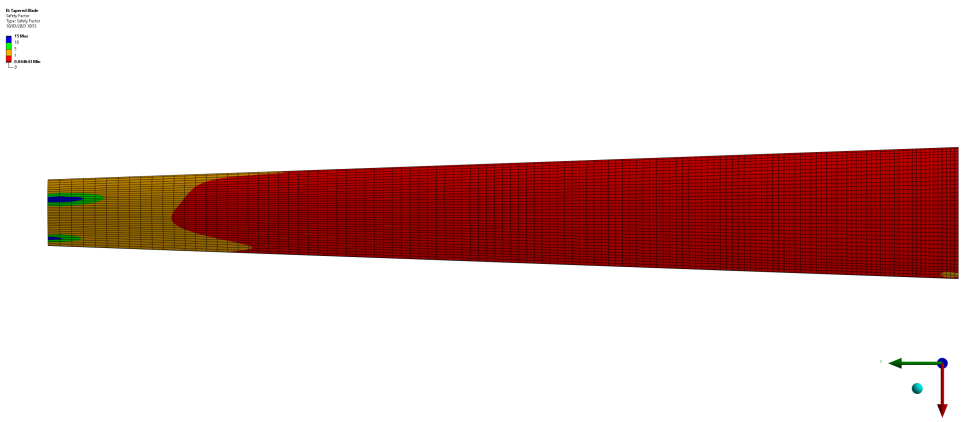

(a) Power model

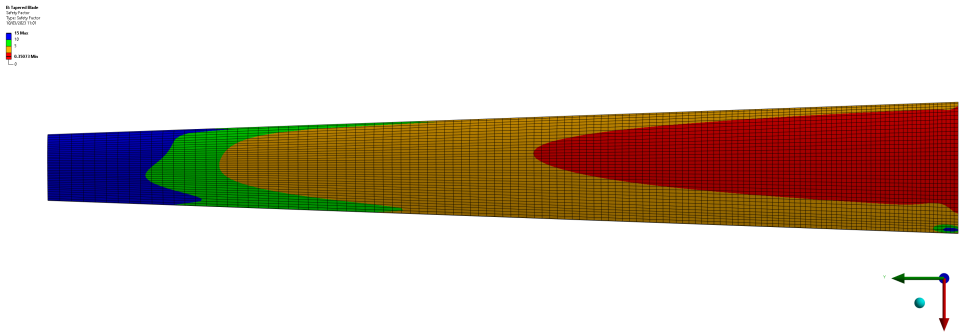

(b) Log linear model

Figure 5.6: Safety factor 1 replacement

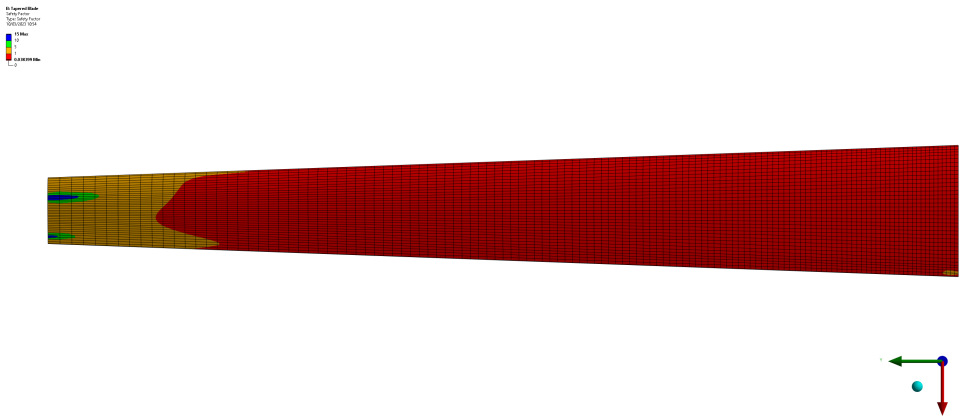

(a) Power model

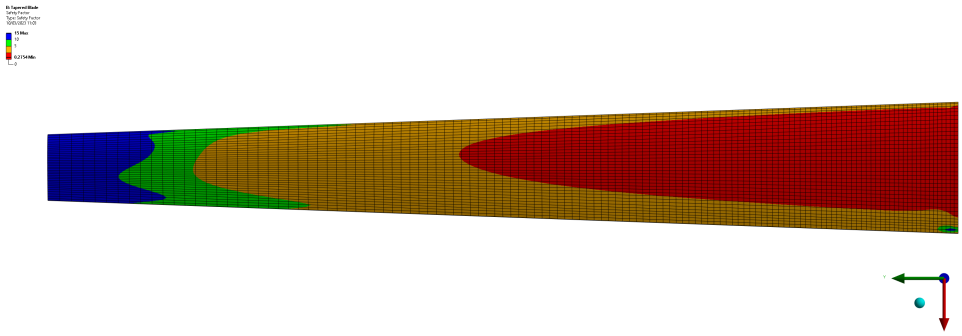

(b) Log linear model

Figure 5.7: Safety factor 3 replacements

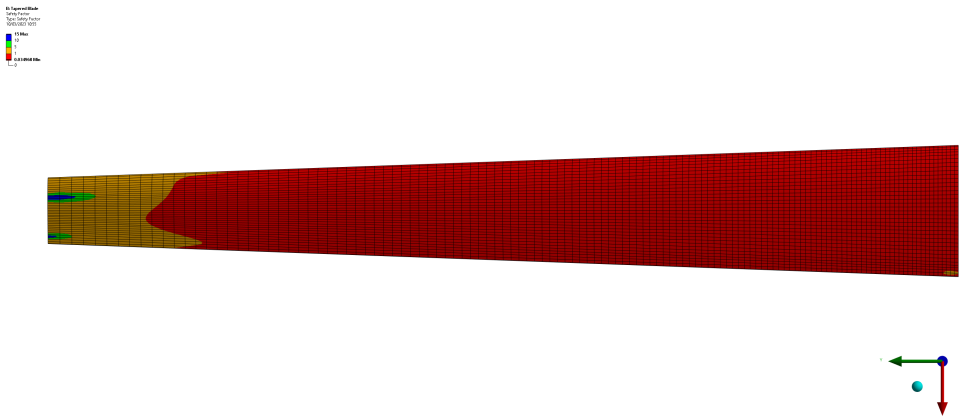

(a) Power model

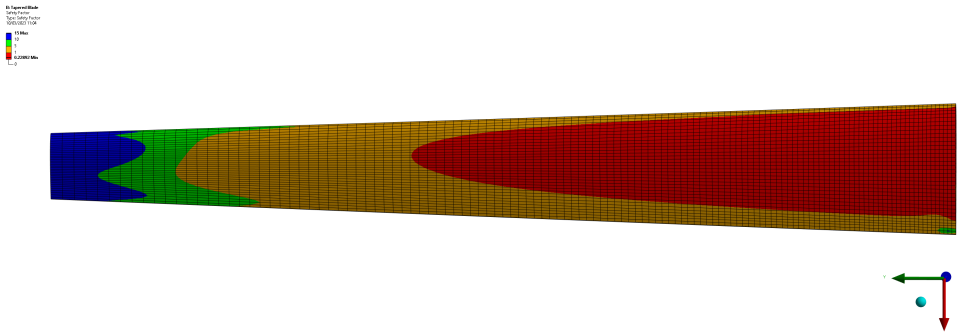

(b) Log linear model

Figure 5.8: Safety factor 5 replacements

5.2.4 Blade design geometry

The results displayed herein are that of the tapered blade with a 5° twist applied to the tip of the device. The results obtained are as seen in Table 5.8, these are both for an orthographic material and a full layup sequence.

Profile	Method	Value	Unit of measure
NACA2415	Orthotropic	12.155	mm
	Layup sequence	12.999	mm

Table 5.8: Composite full blade

Regarding the two types of material applied the overall difference between the values is 6.94%. The result of the structural rigidity of the device increasing is expected. Figure 5.9 shows the deflection over the span of the device.

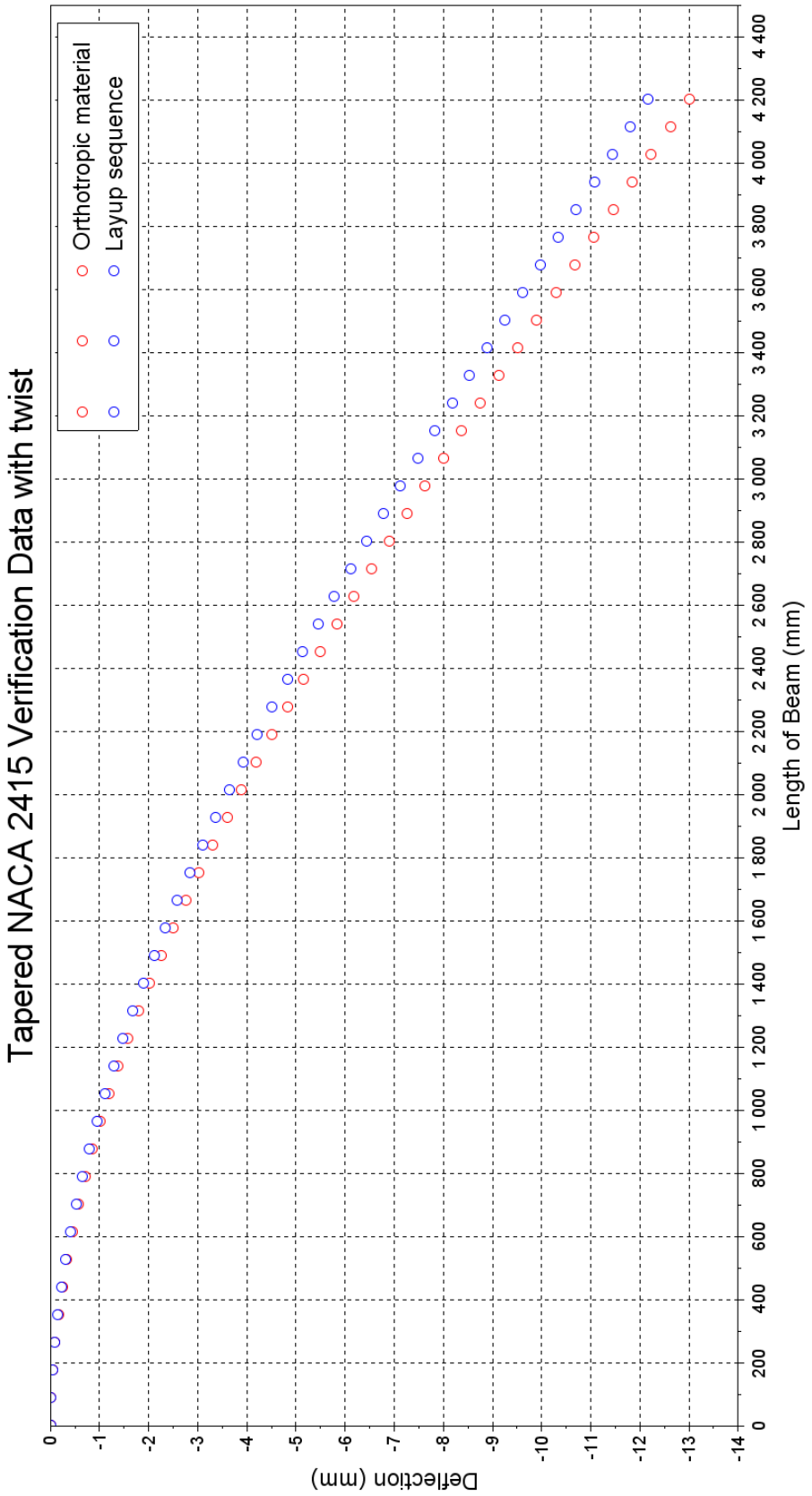

Figure 5.9: NACA 2415 Bending with taper & twist

5.2.5 Blade fatigue modelling

Applying the same principals for fatigue as the tapered blade, the force required to achieve the assumed mechanical factor of safety of 2 the results obtained are found in Tables 5.9 & 5.10.

Number of replacements	Power	Log Linear
1	2978.4	4.55×10^6
3	2628.6	3.07×10^6
5	2443.3	2.44×10^6

Table 5.9: Minimum blade life

Number of replacements	Power	Log Linear
1	0.044	0.35
3	0.038	0.27
5	0.034	0.22

Table 5.10: Minimum blade factor of safety

The blade was also tested for 1 & 5 replacements using the same boundary conditions as the regular tapered blade; Table 5.11 shows the resulting data when a 1400 Newton load is applied. When performing this experiment, the stress factor of safety increased to 2.33. Figures 5.10 & 5.11 display the location of minimum factor of safety during the simulations.

Number of replacements	Power		Log Linear	
	Life	Factor of safety	Life	Factor of safety
1	5141.5	0.051	1.28×10^7	0.399
5	4085.6	0.039	6.45×10^6	0.261

Table 5.11: Minimum blade factor of safety

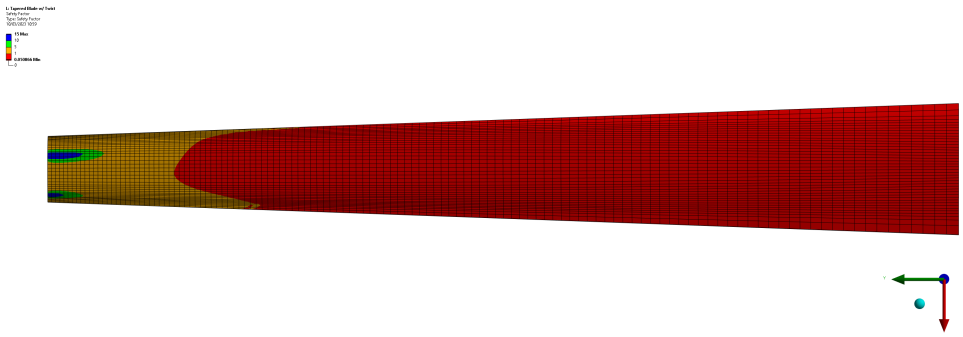

(a) Power model

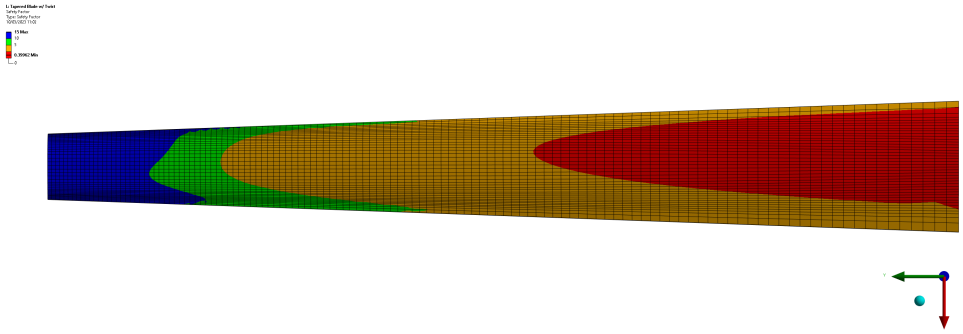

(b) Log linear model

Figure 5.10: Safety factor 1 replacement

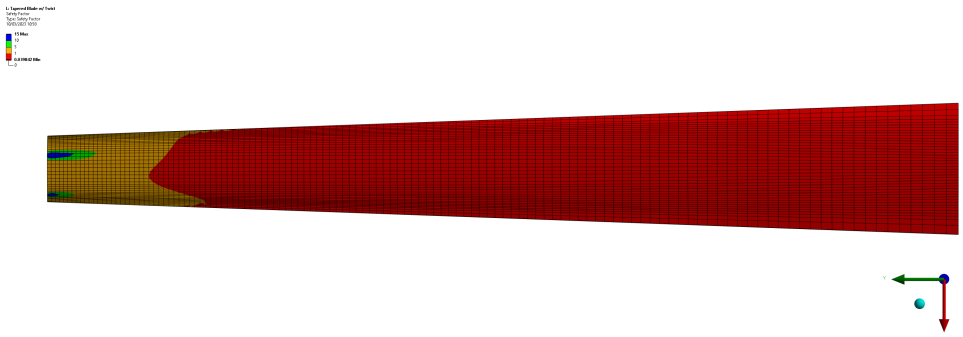

(a) Power model

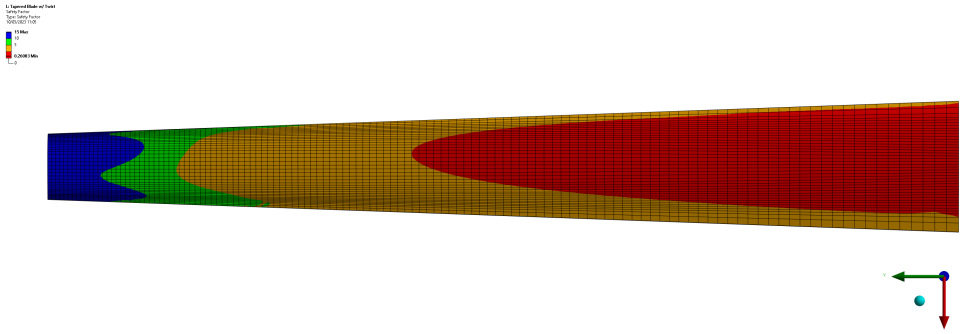

(b) Log linear model

Figure 5.11: Safety factor 5 replacement

Chapter 6

Discussion

This section of the thesis examines data in order to demonstrate the key findings for this research. Thereafter, the opportunity to display the analysis of these data will be investigated, exploring the errors between the key findings presented; giving value and context to the generated results.

6.1 Composite material properties

A key part of this research is the development of realistic composite materials to use within later experiments of the blades. The results calculated for these has been done utilizing a varied approach to general results, one being a test of classical lamination theory while 2 of those being FEA simulations. The purpose of producing different methods of calculating the overall material properties is to ensure that during later modelling stages such as blade bending that the material applied to the structure is one of confidence and reliability due to the rigorous testing done during these experiments, therefore allowing the results of bending to be validated. The different methods supplied have involved a CLT code produced in SciLab while ANSYS APDL used a specified SHELL281 element type and SHELL181. ANSYS Workbench is set to automatically select the element type based on the meshing procedure; this resulting in SHELL181. APDL had SHELL281 selected due to the number of degrees of freedom at each node, with a total of 8 nodes. This allows the element type to be used for modelling layered structures such as composite materials or even sandwich construction.

Here, the key results is overall material properties, which demonstrates that varying shell types may be employed to model accurately the behaviour of composites *in silico*, further enhanced with a calculated model of classic lamination theory. The calculated Young's modulus for the overall composite material returned a result of 12.786 GPa in all three

methods, shown in Table 5.1. The manner in which the results from FEA have been calculated utilized a 0.1% stain placed in either the x or y axis of the system to produce a displacement of the token therefore allowing for a calculation of the strain, seen in equation (2.2). It is important to note that the displacement has been applied to either x or y at one time. In order to calculate the Young's modulus for the composite token, the resulting stress caused by the displacement had to be measured. The approach used to do this involved producing a force from the system using a reaction force from the displacement and knowing the area in which this is acting allows for a fully compliant equation (2.1). Here these results have been used within equation (2.3). CLT run through SciLab has the full lay-up sequence data input into the system along with the individual mechanical properties for the two materials within this glass fibre. This allows the full CLT code to run through resulting with the A, B, and D matrices being produced, seen in equation (3.31). The matrices have been produced using equations (3.32), (3.33), and (3.34). Once these matrices have been calculated, the Young's of the composite has been found using the inverse of the A matrix while both equations (3.35) & (3.36) are employed. During this stage of the material modelling is was found that the full CLT is not well documented within literature as the Reuters matrix shows. This is not found in subject area literature such as Gibson [40] where the stage of the Reuters matrix is seen as a correction factor rather than a key to the theory as mentioned by NASA [66] & David Roylance [41].

Further to the Young's modulus of the composite being calculated the Poisson's ratio has been calculated to be 0.303 for two methods while ANSYS Workbench supplying the Poisson's as 0.3 resulting in the largest percentage difference within all of the results being 1%. The results gathered indicate that all methods used still yield an accurate Poisson's ratio due to the low percentage difference between the data. The results are generated using equation (2.4), where these strains are gathered from FEA simulations as the change in length in the different axis; again using equation (2.2). In order to calculate the overall Poisson's ratio of the composite material through CLT in SciLab utilizes the inverse A matrix calculated earlier in the process and taking positions A_{11} and A_{22} as seen in equation (3.39).

As seen in the above and Table 5.1 the results gathered using the different methods shows the little to no difference within the numbers leading to believe that the data indicates the successful modelling of a composite material in order to find full composite material properties using varying approaches with very little suspicion that these data could be unreliable. Although these approaches may have been carried out before, the results show that there is a deep reliability within the data presented and to be taken forward on to the application of the blades. The key areas from this part of the research show that a composite material

may be modelled using different SHELL elements within ANSYS to yield the results while also correlating with CLT, this shows that within CLT and ANSYS any composite material may be modelled to verify its full mechanical properties.

6.2 Full layup sequence & orthotropic material

A key finding during this research is the similarity of results during bending of composite materials when applied as both a full layup sequence and as an equivalent orthotropic material. Throughout the modelling processes each experiment run had a number of different approaches, these included ones such as: geometry; with both a full lay-up sequence applied and the equivalent orthotropic material, as well as equivalent geometry; in terms of a box section with the full layup, and orthotropic materials. This similarity is also seen during different blades types: straight, tapered, and twisted were all subject to the same phenomena.

The first experiment that highlighted this similarity is the straight blade tests where the blade was subject to a 1000 Newton load the maximum displacement returned for the layup is 111.19mm, while the orthotropic value is 114.51mm. The difference between these two mentioned values is 2.99%, this would suggest that the maximum displacement of the blade can be modelled as either a layup sequence composite or an orthotropic equivalent. Further to this finding, the displacement over the span of the blade is also comparable between the two material applications, Figure 5.3 shows the close paths of both materials.

The same can be seen when moving forward to the tapered blade structures, the geometry was subject to a 100 Newton load as this is presentable to average forces seen during operation, as seen from equation (4.9). When applying this force to the structure the results are 13.01mm maximum displacement for the layup sequence while the orthotropic is 12.16mm. This calculates a difference in the values to be 6.53%, again showing that the results are comparable for the two material types. However, this is also seen on the equivalent box section for the geometry, the layup sequence returned 13mm while the orthortropic came back as 12.15mm, the percentage difference between these values is 6.47%. This is almost the same percentage difference between the two materials and two geometry types. The displacement over the span of the blade, also confirms a similar pattern to that of the straight blade, that being the is also comparable over the span.

The final instance this phenomena is observed is during the testing of the tapered blade with the twist applied to the tip. Utilising the same 100 Newton load, the results are very similar to the non-twisted blade. The layup sequence had a maximum displacement of 13mm while the orthotropic had a maximum value of 12.155mm. As mentioned within the results,

this means a percentage difference of 6.49%.

Overall, the results of both the layup sequence and equivalent orthotropic material was as expected regarding the similarities of the deflections. This again demonstrates that the composite material has been created in a manner that is representative of an orthotropic equivalant. It should be noted that as long as the equivalent orthotropic composite material can generated effectively, it may be an approach to be considered if the subject of testing and research is not that where the focus is the material itself.

6.3 Wind Turbine Blades

The main subject of this research being wind turbine blade, this section will be discussing the results of the blade testing within each section. This will include the geometry, materials, and numerical modelling i.e the Runge-Kutta being used. The discussion will follow the order in which the results have been produced.

6.3.1 Straight

The research on blades began with an initial study into blades with a consistent chord length, therefore the blade being straight. The research has identified the 2 airfoils that would be ideal to use within the research; these being NACA2414 & NACA2415, the former being the subject of previous research within JTi. The first stages of the blade testing is required to identify from the two airfoil profiles which is the more structurally sound in order to take this profile forward into the remaining research. In order to gain results that would not have involvement from previously modelled composite materials, it is decided that these tests would be conducted using the available material library in ANSYS Workbench to selected the general aluminium alloy available. The material properties this used are found in Table 4.5. To gain an understanding of which of the profiles had more structural withstanding, a force of 1000 Newtons is applied as a UDL while having the beam fixed at one end, creating a cantilever beam. The remaining tests performed on the blades are as cantilever beams and UDLs applied. This results gathered from these simulations yielded that NACA2415 appears to have less deflection at 18.660mm compared to NACA2414 which was 21.355mm. The difference in maximum displacement values obtained through ANSYS Workbench is calculated to be 14.4% more from NACA2414. In order to ensure that the results are valid, a cantilever beam has been modelled in SciLab using equation (3.1), the second moment of area is calculated from separating the coordinates of the profiles into x and y axis data points. Further to this, the Y values are separated into upper and lower values, these values are

then used to compute the area of the blade using the arc length. The results obtained show that ANSYS Workbench was accurate with the results gathered. The uniformly distributed cantilever beam calculated the maximum displacement for NACA2415 to be 19.439mm, 4.17% difference from ANSYS Workbench. While NACA2414 is calculated at 22.262mm, resulting in a percentage difference of 4.24% when compared with ANSYS Workbench. NACA2415 is deemed the more structurally sound due to both methods of experiments not only producing similar results but with clear evidence that this profile deflects much less under the same conditions. This is further back up when looking at the deflection over the span of each profile. Figures 5.1 & 5.2 show that over the span of the blade the again, NACA2415 deflects less than NACA2414.

The next section of the straight blade modelling is to take the successful airfoil profile forward for the remaining research experiments, here the composite material is applied to the blade for the first time during the research. Whilst continuing with the 1000 Newton UDL applied to this the material has been changed to the composite material in both an orthotropic manner as well as the full layup sequence. To ensure that the modelling has been carried out with rigour, an equivalent box section has been modelled as well as the introduction of the Runge-Kutta for the application of the composite material. Introducing these methods allows for a full in-depth analysis of the structure and the material. Applying the new material to the geometry, the results returned as 12.16mm and 13.01mm for orthotropic and the layup sequence respectively; this leads to a percentage difference of 6.53%. The addition of the further experiments such as the Runge-Kutta, bending theory, and equivalent box section shows a trend in the data The Runge-Kutta brings a value of 111.31mm, bending theory obtained 109.97mm, while the equivalent box section had a maximum displacement of 109.56mm; these values can be found in Table 5.3. Looking between the FEA results, this concluded the largest percentage difference of all the results being 4.3%, and the numerical experiments the percentage difference value is 1.2%. When comparing all of the data of this experiment it suggests that the experiment performed has results that are not only reliable but also verified and validated. This statement is further backed up when looking into the displacement of the blade over the span, Figure 5.3 shows the similarities of the data where bending theory and the box section appear to be the more stiff of the approaches.

6.3.2 Tapered

Continuing the blade studies the geometry has been updated to introduce a tapering effect of the blade, the taper is at a scale of $1 : 0.5$ from the tip to the root of the blade: Figure 4.10a shows the tapering effect with displaying the mesh of the blade. The tests performed

on the following structures has been calculated using the wind force calculation, equation (4.9). The wind force calculation has been based on a Class II system where the average wind speed experienced by the blade is 8.5 metres per second. This translates into a force of 81.9 Newtons which is further increased to 100 Newtons so the bending experienced by the blade is a more extreme manner when compared to regular service. The importance of this is to develop models of these blades under loading conditions that could introduce fatigue into the system by increasing the forces applied this should have the desired affect. The resulting bending both at maximum and over the span of the blade followed a similar trend.

The FEA results came back with a maximum displacement of 13.01mm when modelling the full layup sequence, meanwhile the equivalent box section returned the lowest maximum displacement of 12.15mm, a percentage difference of 6.6% over the whole result set. The general trend from the FEA results seen in Table 5.4 shows that the orthotropic material and layup sequence reduce the maximum displacement of the blade when altering the geometry to the equivalent box section, the largest change seen in the results is 0.02mm, a percentage difference of 0.15%. This finding suggests that in the event of modelling these devices it would be appropriate to model the equivalent box section in order to return an accurate simulation of these devices in bending; this is a more efficient method as the model is more simplistic. Overall, the results obtained through these simulations did not return any unusual or abstract data as the maximum bending achieved had a total difference of 6.6%, suggesting that the data is accurate and reliable. Here we see the introduction of the Castigliano's method which has only returned a result of maximum bending, however, this is supplying a bending value with a difference of 0.8% to the previously tried Runge-Kutta method. Further data also supports that the findings are dependable as over the span of the blade, the bending profile of the blade follows the same pattern while remaining within close values of each other, only becoming more spread towards the tip of the blade where the maximum displacement has been calculated. The overall finding from this work is that the bending of these blades during more extreme force cases, these would be deflection less than 1% of the span of the blade, this would suggest that these devices are designed in a manner to sustain more extreme weather conditions therefore designed for purpose.

6.3.3 Twist

To aid in the formation of a more representative picture of the displacement in practice, the geometry has been updated to provide an enhanced model. The geometry in question is an updated version of the tapered blade, whereby a twisted element has been introduced at the tip of the blade. The manner in which this has been implemented is to adjust the angle of

the airfoil at the tip of the blade, this introduced a 5° rotation of this profile. Once in place the leading edge of the blade is at a 5° angle from the chord of the root of the blade, as seen in Figure 4.12. Utilising the same loading conditions from the tapered blade, the deflections both as maximum at the tip and over the span of the blade have been captured. At this stage of the research it is also found that due to the previous accuracy of the models, both FEA and numerical, being within an acceptable percentage of one another, in this case FEA is the only method explored. As before, the full 40-layer layup sequence and the equivalent orthotropic material has been applied to the new geometry. The maximum deflection of these blades is both 12.155mm and 13mm for the orthotropic and layup sequence materials respectively; the overall difference of these values is 6.94%. The results returned are expected, as these are in a similar range to that of the blade with a taper but no twist.

Comparing this with the the previous model, without the twist, the displacement is reduced by a small amount. Comparing the two layup sequenced models, the displacement is reduced from 13.01mm to 12.999mm when adding the twisted section, a reduction of 0.084%. Meanwhile, the orthotropic materials have experienced a similar trend; without the twist the deflection was 12.16mm while with the twist this is reduced to 12.155mm; this being a reduction of 0.04%. Although the displacement values are similar with very little change, this is an expected result as this will increase the structural stiffness of the device while in bending. This would reflect industry practices as these models are more representative of real world devices, as the twisted angle increases, the devices deflection would decrease under load.

6.4 Stress comparison

One of the discoveries during this research is the manner in which the stress calculations can be employed irrespective of the modelling software. Throughout the research, a multitude of methods have been utilized to generate blade models with a variance in the geometry characteristics. This is proven during the methods used within the research, these being ANSYS APDL & Workbench and CLT. CLT is employed through SciLab, where this has been used to further deepen the validation of the composite material and the bending of these materials through ANSYS. As the Wind Turbine Blades section has discussed, the results for the bending using a verified material have been in an acceptable range of one another; the largest being 6.6%. Although, within the use of CLT this alone will not be able to incorporate the bending of the composite materials, hence the introduction of both EB beam theory and Castigliano's theorem, where by the only difference is that Castigliano's

introduces the fictitious moment at the end of the beam. EB beam theory is considered the classic method for this approach as it often referred too as the 'bending triple', where the CLT has been used to develop the material properties which are used to calculate bending through the stress values. Castigliano's is employed at this stage to provide a verification of the EB beam theory, the difference between the theories is that Castigliano's can only return the maximum displacement on the blade. The resulting values of these two methods can be seen in Table 5.4, where EB beam theory returned a value of 12.52mm while Castigliano's is 12.63mm; thus a total varience of 0.88%.

6.5 Fatigue

Another key section of the research involves developing a fatigue model for the blade when running at a mechanical stress factor of safety value of 2. This part of discussion will make comment on remaining life of these devices in both tapered with and without the twisted section. In order to ensure the mechanical stress factor of safety to be equal to 2, the tapered blade was subjected to 1400 Newtons, while the twisted blade 1600 Newtons. The twisted blade was also subjected to identical loading to that of the tapered blade to be able to develop a comparison case. All minimum life values are located towards the root of the WTB as expected.

The results to be discussed have not taken into account the typical fatigue models of Goodman, Soderberg, and Gerber. It is worth noting that with the application of these theories, Goodman and Soderberg become the same with the assumptions applied. The assumptions are: the yield strength of the material is that of the tensile strength and that the strength of the material at the number of cycles to failure is 1% of its original value. Equations (6.1), (6.2), and (6.3) outline these theories:

$$\sigma_a = \sigma_N[1 - \frac{\sigma_m}{\sigma_{TS}}], \tag{6.1}$$

$$\sigma_a = \sigma_N[1 - \frac{\sigma_m}{\sigma_y}], \tag{6.2}$$

$$\sigma_a = \sigma_N[1 - (\frac{\sigma_m}{\sigma_{TS}})^2], \tag{6.3}$$

where σ_a is the stress amplitude, σ_m is the mean stress, σ_N is the stress at the number of cycles to failure, σ_y and σ_{TS} are as previously mentioned assumed to be equal, here this is the matrix material of the composite. The overall result when applying these would indicate

that for Goodman & Soderberg the values are 75% correct in comparison to these results, with Gerber being 93.75% correct. Another aspect to be noted that has not been covered within the proceeding results is the correction for the twisted blade section, where this has been stated to potentially reduce by up to 50% with this type of geometry [72].

6.5.1 Tapered blade

One of the geometries simulated is that of the tapered blade without the twist. The results show that the number of cycles left within the device are substantially different between the methods applied. The Log Linear models returned minimum blade life within the millions of cycles, displaying a total percentage difference between 1 and 5 replacements of 87.5%, while the Power results came back as thousands with a total percentage difference between 1 and 5 replacements of 21.9%. When comparing these with one another, the difference within would result in large percentages due to the vast difference within the life remaining calculated from each methods. The same applied to the Factor of Safety (FoS) of these, although these all suggest total failure of the device has occurred. The Power model saw a minimum FoS of 0.04 during the 1 replacement tests, while during the same simulation the Log Linear model displayed a FoS of 0.35, the trend is somewhat the same for all of the tests done. Table 5.7 shows the full results. The largest difference between the values is during the 1 replacement where this results is approximately 8 fold. Overall, it is not clear which would be the appropriate method to apply for the fatigue calculations of WTBs.

6.5.2 Wind turbine blade

The second of these geometries subjected to fatigue testing is that which contains the twisted nature. As with the non-twisted section the same pattern can be seen with the results, showing that all of the devices would have failed under the conditions and assumptions made. As with the non-twisted section, the minimum blade life remaining in the structures is millions of cycles for the Log Linear method while Power remains within the thousands. With regard to the Power model, the overall percentage difference is the same as the non-twist with a value of 21.9%; meanwhile for the Log Linear model, this percentage difference decreased to 46.4%. When looking into the FoS for each model, these are identical to that of the non-twisted device, this is of particular interest and should be explored within further work. The twisted section also underwent testing in identical conditions to that of the non-twisted blade, this is mentioned within earlier results chapter. The aim of this experiment is to allow a direct comparison of the fatigue values where only geometry varies. The simulations looked

at only the 1 and 5 replacements, here the results indicate that twisted device is more capable of withstanding fatigue when compared to that of the non-twisted device. The Power model saw an increase of 21.6% and 12.8% in the FoS for the 1 and 5 replacements respectively. In comparison to the Log Linear model which displayed an increase of 12.3% and 15.7% of FoS for the 1 and 5 replacements. Regarding the minimum life remaining Power saw an 41.3% and 39.5% increase while Log Linear is over 1.5 fold for 1 and 5 replacements. These results are further back with the results of the bending under identical boundary conditions in which the twisted blade section resulted in left deflection. These result further suggest that the option to specify wind turbine system with WTBs containing a twisted section is not purely for aerodynamic advantage, but also to obtain structural soundness within. Although, it is also not clear which method of fatigue is the appropriate one to apply to WTBs, further work is required within this area of research.

Chapter 7

Conclusions & Recommendations

This final section includes a summary of the work and how the aims originally set out have been met. In the later part of this section recommendations will be made as to where the work can be taken in the future when it is to be continued.

7.1 Conclusions

The concluding section to this work will be demonstrating the aims and objectives set out at the start of the project have been met and the research hypothesis has been proven, via the use of key results found during the employment of the methods chapter 4. As discussed in the previous chapter, the key conclusions are as follows:

- CTL can be used to introduce verification of orthotropic models, as seen in Table 5.1. Whereby the results for both APDL (SHELL281) Workbench (SHELL181) are the same which is further verified through the CLT code run though SciLab.
- Token pieces can be used to determine composite material properties, furthermore to the above statement, the geometry used for both of the FEA methods is the same yielding the same results while utilizing different shell elements for the models, APDL used SHELL281, while Workbench used SHELL181.
- Layup sequencing of composites yields similar results to the orthotropic equivalent, evident throughout the results of bending of the turbine blade, it is seen that the results between the applied layup sequence and an orthortropic equivalent return similar deflection values both maximum and over the span of the blade.

- Introducing the twist affects the deformations of the blade, compared with previous models. The twist adds structural stiffness over the span of the blade when compared to the untwisted blade model. Thus, also affecting the devices ability to withstand material fatigue during service.

- Stress calculations are the same irrespective of modelling software employed, this is proven utilizing a mixture of modelling methods such as ANSYS APDL, and Workbench with the inclusion of the CLT code in SciLab.

7.2 Further work

After seeing how the project has met all of the aims set out, if the work is to be continued there are a number of tasks that would help the research and allow the project to become more rich in the development of wind turbine blade modelling processes and procedures. Firstly, the verification of the twisted blade model, using a similar approach to that of the methods section. A second task that would follow on from that presented in this work would be to further analyse the fatigue of the blade using different simulation methods. For example Fluid Structural Interaction (FSI) studies allowing the wind to produce a pressure on the blade as a fluid, this result would then be supplied to a structural solver where this is applied, as a pressure, to model a bending in the blade. Further, to these, increasing the depth of the material testing through the testing of real world composite structures to validate the work carried out in this thesis. This in-turn supporting the work within this thesis of the material modelling summed up within the conclusions of the work. The final area in which the work could develop, would be the development of realistic wind turbine blade geometry including that of the mounting fixtures to the hub and remaining system. Allowing for further development of the stresses within these structures. Overall, these recommended further works are subject to other Masters research projects within JTi, and should develop solutions to these further works mentioned.

Some of the socioeconomic aspects this research has generated includes the motivation for further research of this work into the design, material, and fatigue of these devices. Further research has already begun wherein Mr. L Waugh is looking at the material properties and how these can be replicated in real world applications. The research group, JTi, is also generating project ideas, aims, and objectives for further research into the subject areas for a number of projects at varying levels such as bachelors and masters degrees. Namely, Mr M. Walsh & Mr C. Howard looking more in-depth of the fatigue of the structures and where this occurs within. Mr A. Tring is looking into how vertical wind turbines could be improved

using recycled materials. The mentioned projects are linked to this research, showing that a result of this is challenging the cultural attitudes of these individuals as well as leading to decision making occurring, not only within the group but the research itself.

Furthermore, generating more research motivation with JTi, some of the other socioeconomic aspects of the project include the relation to the changing of blades during the lift time of the devices, as seen in the results of this research the blades are designed to withstand the typical forces when subjected to normal operating conditions. The follow on factor of this could reduce the number of blades used by a system during the life span unless excessive damage or reason would require the blade to be changed. In turn, the reduction of blade changes will also reduce the costings for businesses and reduce the number of blades needing to be manufactured for the system.

As an outcome of the work presented within this thesis, the wider community has developed a deeper understanding of the problems explored within this work as well as the potential economic impacts. The main areas this attends to is the awareness of the current situation of the wind energy business having large amounts of scrap material from wind turbine blades due to replacing them frequently, thus incurring costs. It is also noted that this monetary value comes from replacing the blades frequently. If the research is taken on board then this could reduce these costs as the fatigue shows that under normal operating conditions these do not experience any significant stresses that would be a cause for concern. Upon the change in views of the subject based on the work presented, this could also lead to an impact on the environment. This is caused by the the reduction in blade changes this would require less non-recyclable materials being produced, hence having less structures heading to land and sea fill at end of life. Overall the socioeconomic issues highlighted within this thesis have an impact both the scientific community within the current research group, but also the wider audience where aspects namely attitude of the situation, the challenge of these, the economical, and environmental but arguable the most important being the general understanding and awareness of the problem and solutions.

References

[1] Lystrup. A Brondsted. P, Lilholt. H. Composite materials for wind power turbine blades. *Annual Review of Materials Research*, 2005.

[2] Rogier P.L. Nijssen Brondsted P. *Advances in Wind Turbine Blade Design and Materials*. Elsevier Science & ACM Transactions on Intelligent Systems and Technology, 2013.

[3] Mark J. Schulz P. Frank Pai Anindya Ghoshal, Mannur J. Sundaresan. Structural health monitoring techniques for wind turbine blades. *Journal of Wind Engineering*, 2000.

[4] K. Englund T.A. Tabatabaei S.H. Mamanpush, H. Li. Recycled wind turbine blades as a feedstock for second generation composites. *Waste Management*, 2018.

[5] Jon G. McGowan & Anthony L. Rogers James F. Manwell. *Wind Energy Explained: Theory, Design and Application*. John Wiley & Sons, 2010.

[6] David A. Spera. *Wind Turbine Technology: Fundamental Concepts in Wind Turbine Engineering*. ASME Press, 2009.

[7] S. Woolley. Power up: The worlds most powerful wind turbine generates first electrons. GE Report, November 2019.

[8] E. Hau. *Wind Turbines*. Springer, 2013.

[9] Rajesh Gupta Ram Bajpal, Megha Goyal. Modeling and control of variable speed wind turbine using laboratory simulator. *Journal of Renewable and Sustainable Energy*, 2015.

[10] Energy & Industrial Strategy Department for Business. Uk energy statistics, 2018 & q4 2018. Press Notice, 2018.

[11] Energy & Industrial Strategy Department for Business. Energy trends UK october to december 2020 and 2020. Statistical Release, 2021.

[12] Energy & Industrial Strategy Department for Business. Energy trends UK october to december 2021 and 2021. Statistical Release, 2022.

[13] N.A. Shuaib & P.T. Mativenga. Energy demand in mechanical recycling of glassfibre reinforcedthermoset plastic composites. *Journal of Cleaner Production*, 2016.

[14] P. Jamieson. *Innovation in Wind Turbine Design*. Wiley, 2011.

[15] Q. Wang J. Chen. *Wind Turbine Airfoils and Blades: Optimization Design Theory*. De Gruyter Inc., 2017.

[16] Simon McBeath. *Competition Car Aerodynamics - A Practical Handbook*. Haynes, 2nd edition, March 2011.

[17] Ira H. Abbott. *Theory of Wing Sections*. Dover, 1959.

[18] B. Johnson J.Whitty, T.Haydock and J.Howe. On the deflexion of anisotropic structural composite aerodynamic components. *Journal of Wind Energy*, 2014.

[19] Y. Bazilevs, M.-C. Hsu, I. Akkerman, S. Wright, K. Takizawa, B. Henicke, T. Spielman, and T. E. Tezduyar. 3d simulation of wind turbine rotors at full scale. part i: Geometry modelling and aerodynamics. *International Journal for Numerical Methods in Fluids*, 2011.

[20] D. Todd Griffith and Thomas D. Ashwill. The sandia 100-meter all-glass baseline wind turbine blade: Snl100-00. Technical report, Sandia National Laboratories, 2011.

[21] W.F. Hosford. *Elementary Materials Science*. A S M International, 2012.

[22] Isaac M. Daniel. *Engineering Mechanics of Composite Materials*. Oxford University ASME Press, 2006.

[23] Robert M. Jones. *Mechanics of Composite Materials*. Taylor & Francis, 1999.

[24] George Staab. *Laminar composites*. Butterworth-Heinemann, 2015.

[25] Marcio Loos. *Carbon Nanotube Reinforced Composites*, chapter 2 - Composites, pages 37–72. CNR Polymer Science and Technology, 2015.

[26] S.L. Kakani. *Material Science*. New Age International LTD, 2004.

[27] Vijay Gupta. *An Introduction to Mechanics of Materials*. Alpha Science International, 2013.

[28] A. Tang J. Huang, W. Liu. Effects of fine-scale features on the elastic properties of zero poissons ratio honeycombs. *Material Science and Engineering: B*, 2018.

[29] M.Shaat S. Faroughi. Poissons ratio effects on the mechanics of auxetic nanobeams. *European Journal of Mechanics - A/Solids*, 2018.

[30] R.E. Rocha Teixeira. *Fatigue Analysis of Wind Turbine Blades*. PhD thesis, University of Porto, 2014.

[31] A.M. Sadegh R.G. Budynas. *Roark's Formulas for Stress and Strain*. McGraw-Hill Education, 2020.

[32] N. Nayak G.R. Kalagi, R. Patil. Experimental study on mechanical properties of natural fiber reinforced polymer composite materials for wind turbine blades. *Materials Today*, 2016.

[33] E.M. Boudi A.E. Marjani R.E. Alaoui, H. Mounir. Mechanical performances investigation of new materials for wind turbine blade. Universite Mohammed V - Morocco.

[34] A. K. Mohanty, M. Misra, and L. T. Drzal. Sustainable bio-composites from renewable resources: Opportunities and challenges in the green materials world. *Journal of Polymers & the Environment*, 10(1/2):19 – 26, 2002.

[35] H.G. Kotik and J.E. Perez Ipina. 3d quasi-static strengths and elastic constants of glass fiber reinforced polyester composite extracted from a wind turbine blade. *Journal of Testing and Evaluation*, 2018.

[36] ASTM Standard. D2344/d2344m-16. *Standard Test Method for Short-Beam Strength of Polymer Matrix Composite Materials and Their Laminates*, 2016.

[37] ASTM Standard. D3039/d3039m-14. *Standard Test Method for tensile properties of polymer matrix composite materials*, 2014.

[38] ASTM Standard. D6641/d6641m - 14. *Standard Test Method for Compressive Properties of Polymer Matrix Composite Materials Using a Combined Loading Compression (CLC) Test Fixture*, 2014.

[39] ASTM Standard. D7078/d7078m-12. *Standard Test Method for Shear Properties of Composite Materials by V-Notched Rail Shear Method*, 2012.

[40] Ronald F. Gibson. *Principles of Composite Material Mechanics*. CRC Press LLC, 2011.

[41] David Roylance. Laminated composite plates. Technical report, Massachusetts Institute of Technology (MIT), 2000.

[42] Zhenye Sun, Jin Chen, Wen Zhong Shen, and Wei Jun Zhu. Improved blade element momentum theory for wind turbine aerodynamic computations. *Renewable energy*, 96:824–831, 2016.

[43] Erich Hau. *Wind turbines: fundamentals, technologies, application, economics*. Springer Science & Business Media, 2013.

[44] GAM Van Kuik, Jens Nørkær Sørensen, and VL Okulov. Rotor theories by professor joukowsky: momentum theories. *Progress in Aerospace Sciences*, 73:1–18, 2015.

[45] M. Messina R. Lanzafame. Fluid dynamics wind turbine design: Critical analysis, optimization and application of bem theory. *Reewable Engergy*, 2006.

[46] North Atlantic Treaty Organization. *Fluid Dynamic Aspects of Wind Energy Conversion*. AGARD, 1979.

[47] A. Kolios L. Wang, X. Liu. State of the art in the aeroelasticity of wind turbine blades: Aeroelastic modelling. *Renewable and Sustainable Energy Reviews*, 2015.

[48] S. Voutsinas N. Sorensen H.Aa. Madsen M.O.L. Hansen, J.N. Sorensen. State of the art in wind turbine aerodynamics and aeroelasticity. *Progress in Aerospace Sciences*, 2006.

[49] Junuthula Narasimha Reddy. *An introduction to the finite element method*. New York, fourth edition, 2019.

[50] Clough et al. Stiffness and deflection analysis of complex structures. *Journal of the Aeronautical Sciences*, 23(9):805–823, 1956.

[51] Nic Gaskell. Fluid structural interaction of microarterial anastomoses, 2019.

[52] J. Degroote W.V. Paepegem M. Peeters, G. Santo. High-fidelity finite element models of composite wind turbine blades with shell and solid elements. *Composite Structures*, 2018.

[53] A. Bardsley, J. Whitty, J. M. Howe, and J. Francis. A review of in situ loading conditions for mathematical modelling of asymmetric wind turbine blades. *Fundamentals Of Renewable Energy and Applications*, 2015.

[54] Aman Arora, Aanchna Sharma, Mohit Singh, Dhiraj K Mahajan, and Vinod Kushvaha. Fatigue response of glass-filled epoxy composites: A crack initiation and propagation study. *International Journal of Fatigue*, 170:107542, 2023.

[55] Ciprian Ionut Moraras, Viorel Goanta, Dorin Husaru, Bogdan Istrate, Paul Doru Barsanescu, and Corneliu Munteanu. Analysis of the effect of fiber orientation on mechanical and elastic characteristics at axial stresses of gfrp used in wind turbine blades. *Polymers*, 15, 2023.

[56] C Hemanth Kumar, TS Sachit, and Arunkumar Bongale. Formulation of constant life diagram for fatigue life prediction of glass-carbon/epoxy composites. *Journal of Failure Analysis and Prevention*, pages 1–17, 2023.

[57] Hicham Boudounit, Mostapha Tarfaoui, and Dennoun Saifaoui. Fatigue analysis of wind turbine composite blade using finite element method. *Wind Engineering*, page 0309524X231155549, 2023.

[58] Changduk Kong, J Bang, and Y Sugiyama. Structural investigation of composite wind turbine blade considering various load cases and fatigue life. *Energy*, 30(11-12):2101–2114, 2005.

[59] Tengteng Zheng, Caiqi Zhao, and Jianghui He. Research on fatigue performance of offshore wind turbine blade with basalt fiber bionic plate. In *Structures*, volume 47, pages 466–481. Elsevier, 2023.

[60] V. Gupta. *Introduction to Mechanics of Materials*. Alpha Science International, 2013.

[61] K.H. Lee C.M. Wang, J.N. Reddy. *Shear Deformable Beams and Plates : Relationships with Classical Solutions*. Elsevier Science & Technology, 2000.

[62] Ted Belytschko, Wing Kam Liu, Brian Moran, and Khalil Elkhodary. *Nonlinear finite elements for continua and structures*. John wiley & sons, 2013.

[63] J. Erochko. *An introduction to structural analysis for civil engineers*. Carleton University, 2020.

[64] W. Bolton. *Mechanical Science*. Oxford ; Malden, Massachusetts : Blackwell Publishing, 2006.

[65] M. Petrolo E. Carrera, G. Giunta. *Beam Structures: Classical and Advanced Theories*. John Wiley & Sons, Incorporated, 2011.

[66] A.T. Nettles. Basic mechanics of laminated comosite plate. Technical report, National Aeronautics and Space Administration (NASA), 1994.

[67] J. C. Butcher. Runge-kutta methods for ordinary differential equations. In Mehiddin Al-Baali, Lucio Grandinetti, and Anton Purnama, editors, *Numerical Analysis and Optimization*, pages 37–58, Cham, 2015. Springer International Publishing.

[68] K. A. Stroud. *Advanced engineering mathematics*. Palgrave Macmillan Limited, 2011.

[69] O.C. Zienkiewicz R.L. Taylor, J.Z. Zhu. *The Finite Element Method: Its Basis and Fundamentals*. Elsevier Science & Technology, 2013.

[70] ANSYS. *Mechanical APDL Theory 18.2*.

[71] R.A. Ibrahim. *Handbook of Structural Life Assessment*. John Wiley & Sons, Incorporated, 2017.

[72] T.Dahlberg & A.Ekberg. *Failure Facture Fatigue An Introduction*. Student Litteratur, 2002.

[73] Céline A Mahieux. *Environmental degradation of industrial composites*. Elsevier, 2005.

[74] Daniel Gay. *Composite materials: design and applications*. CRC press, 2022.

[75] P. Gao T. Yu D.K.Y. Tam, S. Ruan. High-performance ballistic protection using polymer nanocomposites. *Advances in Military Textiles and Personal Equipment*, 2012.

[76] J.B. Ransom. Global/local stress analysis of composite structures. Technical report, National Aeronautics and Spac Administraion, 1989.

[77] Massachusetts Institute of Technology. Chapter 6 - eigenvalues and eigenvectors.

[78] Sibin Saseendran, Maciej Wysocki, and Janis Varna. Cure-state dependent viscoelastic poissonâs ratio of ly5052 epoxy resin. *Advanced Manufacturing : Polymer Composites Science*, 3(3), 08 2017.

[79] Ansys. *Mechanical APDL 2020 R1*, 2020.

[80] M.H. Zhang. *Wind Resource Assessment and Micro-Siting*. John Wiley & Sons, Incorporated, 2015.